

Chapter 8

Global electromechanics in infarct heart

8.1 Abstract

To test the hypothesis that alterations in electrical activation sequence contribute to depressed systolic function in the infarct border zone, the anatomical correlation of abnormal electromechanics and the infarct geometry was examined in the canine post-myocardial infarction (MI) heart, using a high-resolution MR-based cardiac electromechanical mapping technique. Three to eight weeks after creating an MI in six dogs, a 247-electrode epicardial sock was placed over the ventricular epicardium under thoracotomy. MI location and geometry were evaluated with delayed hyperenhancement MRI. Three-dimensional systolic strains in epicardial and endocardial layers were measured in five short axis slices using motion-tracking MRI (DENSE). Epicardial electrical activation was determined from sock recordings immediately prior to and following the MR scans. The electrodes and MR images were spatially registered to create a total of 160 nodes per heart that contain mechanical, transmural infarct extent, and electrical data. The average depth of the infarct was $55 \pm 11\%$ and the infarct covered $28 \pm 6\%$ of the LV mass. Significantly delayed activation ($>\text{mean} + 2\text{SD}$) was observed within the infarct zone. The strain map showed abnormal mechanics, including abnormal stretch and loss of the transmural gradient of radial, circumferential and longitudinal strains, in the region extending far beyond the infarct zone. In conclusion, the border zone is characterized by abnormal mechanics directly coupled with normal electrical depolarization. This indicates that impaired function in the border zone is not contributed by electrical factors, but results from mechanical interaction between the ischemic and normal myocardium.

8.2 Introduction

Depressed systolic function in the ischemic border zone with normal perfusion has been recognized for several decades (135). The presence of hypocontractile, border zone myocardium has consistently been substantiated by a variety of modalities, including echocardiography (124, 156), radiopaque bead arrays (163, 238), and most recently, MRI (84, 98, 103, 143). The abnormal mechanics of the border zone is clinically important because it may negatively affect ventricular remodeling and hypertrophy (61, 125).

The mechanism underlying the depressed function in the border zone has been explained primarily by mechanical factors. Most investigators concluded that it results from mechanical interactions, or tethering, between normal and ischemic myocardium (93, 94, 156, 163, 210, 238). However, the abnormal mechanics in the border zone may also involve a contribution of abnormal electrical activation. For example, the timing of electrical activation in the border zone may be delayed by abnormal electrical sequence in the infarct zone and depressed shortening, or relative stretch, in the border zone. A relative delay in electrical activation may augment the depressed function in the border zone, because the myofiber in the border zone has to contract against a higher afterload generated by earlier shortening of remote nonischemic zones.

It was hypothesized that alterations in electrical activation sequence contribute to depressed systolic function in the infarct border zone. To test this hypothesis, the anatomical correlation of abnormal electromechanics with reference to the infarct geometry was qualitatively and quantitatively examined in a canine model of chronic myocardial infarction. A high-resolution cardiac electromechanical mapping technique allowed acquisition of anatomical, electrical, and mechanical data with high precision in a near-simultaneous fashion (88).

8.3 Materials and Methods

All animal protocols were reviewed and approved by the Animal Care and Use Committee of the National Heart, Lung and Blood Institute.

8.3.1 Surgical procedures

Six adult mongrel dogs (18–28kg) were anesthetized with intravenous sodium thiopental (10–20mg/kg), intubated, and mechanically ventilated with a mixture of oxygen, medical air and isoflurane (1–3%). An 8Fr arterial introducer was placed in the left carotid artery through a skin cut down (1–2”) under sterile conditions. The surface ECG and the arterial pressure were recorded throughout the procedure. A bolus iv injection of heparin 1,000 IU and lidocaine 40 mg was administered, followed by a continuous iv infusion of lidocaine 110 mg/hr for the entire procedure. A 6Fr guiding catheter was advanced through the introducer to the left coronary ostium under fluoroscopic guidance, and a balloon angioplasty catheter was advanced to LAD through the guiding catheter over a guide wire (0.014”). The LAD was then occluded at its origin by inflating the balloon. Myocardial ischemia was confirmed with ST-T changes on ECG and transient decrease in arterial blood pressure upon balloon inflation. The balloon occlusion was maintained for a total of 120 minutes. Another bolus iv injection of lidocaine 40 mg was given 15 minutes prior to reperfusion to avoid serious ventricular arrhythmia. All the animals showed frequent ventricular ectopic beats after reperfusion. The catheters and the introducer were removed and the surgical wound closed. The surface ECG was recorded 3–4 times per day for the first 48–72 hours to monitor the baseline rhythm.

Three to eight weeks following MI, the animal underwent a median sternotomy under general anesthesia. The heart was placed in a pericardial cradle, and a multi-electrode epicardial sock consisting of a nylon mesh fitted with 247 silver electrodes attached in an ordered fashion was placed over the ventricular epicardium, as described previously (88). The sock was placed in a consistent and predetermined orientation for all experiments and secured with several sutures. Ten to fifteen 4-mm diameter glass beads (18 μ L) filled with an aqueous solution of gadopentetate dimeglumine (Gd-DTPA) (5mM) were attached to the sock as markers for registering mechanical and electrical data. An MR-compatible pressure micromanometer catheter (Millar, SPC-350, 5Fr) was advanced under fluoroscopic guidance to the left ventricular (LV) cavity through a 6Fr arterial introducer placed in the right carotid artery. A ground reference electrode was sewn onto the fat pad at the aortic root. All sock wires were run directly out of the chest and the animal was transported to the MR scanner.

8.3.2 Data acquisition

MR scanning was performed in a 1.5-T scanner (Siemens Sonata). LV geometry (LV end-diastolic and end-systolic volumes) and function (LV stroke volume and ejection fraction) were evaluated with a cine true FISP sequence (BW \pm 1,395 Hz/pixel, TE/TR 1.9/3.7 ms, readout flip angle 50°, FOV 225 x 300 mm, image matrix 192 x 256, spatial resolution 1.2 x 1.2 x 6.0 mm, 8–10 slices without a gap). MI geometry was evaluated with a phase-sensitive delayed hyperenhancement (DHE) inversion recovery sequence (134) 10 to 30 minutes following an intravenous injection of a contrast agent (Gd-DTPA, Berlex Magnevist) at 0.25 mmol/kg (BW \pm 140 Hz/pixel, TE/TR 3.9/8 ms, turbo flash with readout flip angle 30°, FOV 119 x 200 mm, image matrix 122 x 256, spatial resolution 1.0 x 0.8 x 3.0 mm, readout at late diastole, 13 views per segment, 20–25 slices without a gap). For these two sequences, LV short-axis image slices from the LV apex to base were acquired in a consistent manner based on predetermined anatomical landmarks without gaps between slices. Each image acquisition was ECG-gated, and the image was acquired during a single breath hold (30–40 sec) by manually holding mechanical ventilation at end expiration. Three-dimensional (3D) displacement fields were calculated measured in five short axis slices using a motion tracking sequence (DENSE, BW \pm 1000 Hz/pixel, TE/TR 1.55/3.1 ms, 15° readout flip angle FOV 175 x 350 mm, image matrix 128 x

256, spatial resolution 1.36 x 1.36 x 8.0 mm) (5). To spatially register the displacement fields with the MI geometry, encoding and readout of the DENSE sequence was set at end systole and end diastole, respectively. The timing of end systole and end diastole was determined from the cine images.

The epicardial sock electrical recording system in the MR scanner room was described previously (88). Briefly, all 247 electrodes were radiofrequency-filtered at the MR scanner interface, and the data from the epicardial electrodes and physiological monitoring, including LV pressure and ECG, were simultaneously acquired at a minimum sampling rate of 1,000Hz for a duration of 10 sec immediately prior to and following the MR scans (29). Animals were euthanized and their hearts were scanned with a 3D spin-echo sequence to locate the glass bead markers (BW \pm 130 Hz/pixel, TE/TR 12/148 ms, FOV 256 x 256 x 88 mm, image matrix 256 x 256 x 88, spatial resolution 1.0 x 1.0 x 1.0 mm). After excision, the heart was filled with vinyl polysiloxane, maintaining end diastolic shape, and the locations of electrodes and beads were digitized (Microscribe 3DLX, Immersion Corporation, San Jose, CA) (88, 148).

8.3.3 Data analysis

The LV myocardium was manually segmented in the DENSE images. The 3D end-diastolic configuration and 3D displacement of the tissue in each pixel were measured (4). The end-systolic configuration was calculated from the displacement vector field and the end-diastolic configuration. The Lagrangian Green's strain tensor \mathbf{E} was calculated in every tetrahedron of adjacent 4 pixels in the LV myocardium as $0.5(\mathbf{F}^T\mathbf{F}-\mathbf{I})$, where \mathbf{F} is the deformation gradient tensor, \mathbf{F}^T is the transpose of \mathbf{F} , and \mathbf{I} is the identity matrix. The reference and deformed states were defined as end-diastolic and end-systolic configurations, respectively. Three independent finite strains (E_{rr} , E_{cc} , and E_{ll}) were computed in the local cardiac coordinate system with reference to the center of mass of each short-axis LV myocardium image (172). E_{rr} , E_{cc} , and E_{ll} reflect myocardial stretch or shortening along the radial (E_{rr}), circumferential (E_{cc}) and longitudinal (E_{ll}) cardiac axes, respectively. The LV circumference was divided into 32 sectors and two layers (endocardium and epicardium), and average strain values were calculated in each sector.

In the DHE images, MI geometry and endocardial and epicardial borders were manually segmented (164). As in the strain map, the LV circumference was divided into 32 sectors, and the average transmural depth of MI was calculated in each sector. The values were linearly interpolated to determine the MI depth at the DENSE image slice positions.

Electrical signals from the 247-lead sock electrodes were averaged over approximately 20 consecutive heartbeats. The local depolarization time at each electrode was defined as the peak negative dV/dt within the QRS complex (140). The time reference for the local depolarization times was the earliest ventricular depolarization time in each heart. Delayed electrical activation was defined as electrical activation time exceeding the mean +2SD of activation times of all the nodes. Electrical maps were spatially referenced to the strain and MI geometry maps using the least squares fit of glass marker beads (88, 148). The electrical activation time in each of the 32 sectors was calculated as the weighted average of the electrical activation time at three adjacent electrodes (Figure 8-1). In essence, the electrical activation at 160 (= 32 sectors x 5 slices) nodes was calculated from those at the 247 original sock electrodes. A total of 160 nodes that contain mechanical, infarct extent, and electrical data were measured.

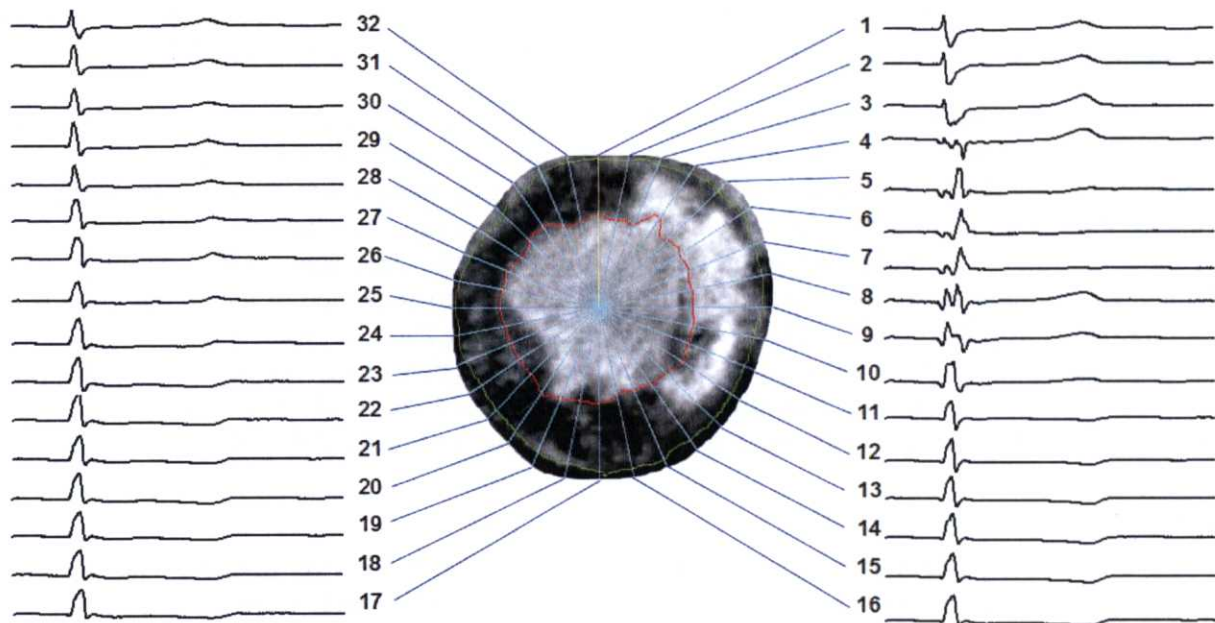


Figure 8-1: Epicardial electrical signals during a cardiac cycle (cycle length = 544 msec, HR = 110 bpm) registered to a short-axis delayed hyperenhancement (DHE) MR image of the LV split into 32 sectors. Regions of bright intensity correspond to MI. In this image, abnormal or delayed activation is seen from sectors 4 through 9, whereas the infarct ranges from sectors 3 through 14.

At the mid-LV level, each sector corresponded to an approximate 3-D dimension of 6 mm (circumference), 6 mm (longitudinal), and 10 mm (radial). The infarct zone was defined as the sectors including MI. The border zone was defined as the sectors immediately adjacent to the infarct zone, and the remote zone was defined as the sectors opposite to the infarct zone in the short-axis images. Division of the LV circumference into 32 sectors was chosen to create nodes with sufficiently high spatial resolution that would robustly detect the depressed function at the border zone, the width of which is reported to be <10 mm (93, 94, 156, 198, 210, 238).

8.3.4 Statistical analysis

Values are means \pm SD unless otherwise specified. A paired t-test was used to compare electrical and mechanical parameters. Statistics were performed using SigmaStat 3.0 (SPSS, Inc. Chicago, IL).

8.4 Results

All the animals went into intermittent ventricular tachycardia 24 hours after reperfusion, which lasted for 24-48 hours, and normal sinus rhythm resumed thereafter. The animals underwent the electromechanical data acquisition 38 ± 12 days post-MI. Hemodynamic parameters at the time of the electromechanical data acquisition are summarized in Table 8-1.

8.4.1 Infarct map

The infarct was located in the anteroapical region, and usually involved the anterolateral papillary muscle on the endocardial border (Figure 8-2). The epicardial border exhibited spatially intricate structures with multiple interdigitations of viable myocardium within the infarct zone.

The average depth of the infarct was $55 \pm 11\%$ and the infarct covered $28 \pm 6\%$ of the LV mass (Figure 8-3A).

Heart rate (bpm)	121 ± 19
LVP _{max} (mmHg)	85 ± 16
dP/dt _{max} (mmHg/s)	1713 ± 661
dP/dt _{min} (mmHg/s)	-1515 ± 643
LVEDP (mmHg)	7 ± 3
LVEDV (mL)	40 ± 6
LVESV (mL)	23 ± 5
LVSV (mL)	17 ± 2
LVEF (%)	43 ± 3
CO (mL/min)	2058 ± 517

Table 8-1: Hemodynamic data. Values are mean \pm SE. LVP_{max}: peak LV pressure, dP/dt_{max}: peak positive dP/dt, dP/dt_{min}: peak negative dP/dt, LVEDP: LV end-diastolic pressure, LVESV: LV end-systolic pressure, LVSV: LV stroke volume, LVEF: LV ejection fraction, CO: cardiac output.

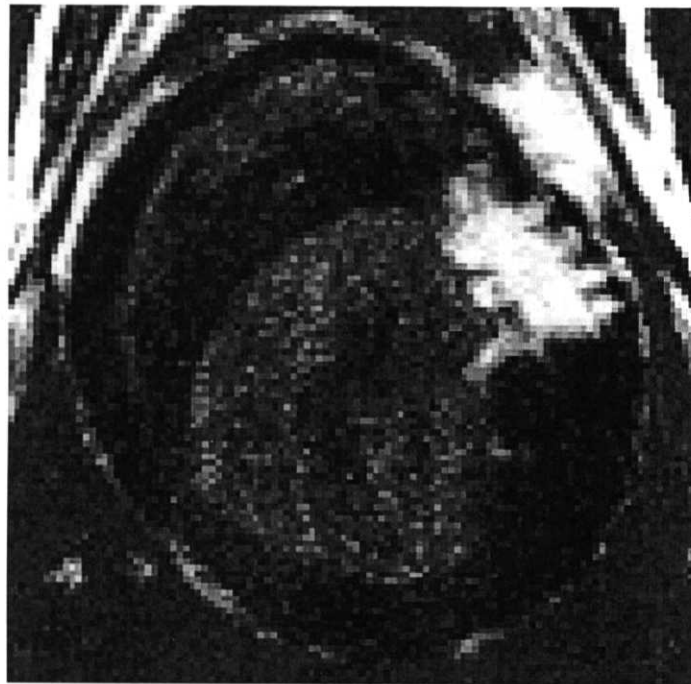


Figure 8-2: Short-axis, delayed hyperenhancement (DHE) image of MI from a single animal. Regions of bright intensity correspond to MI. Note multiple interdigitations of viable myocardium within the infarct region.

8.4.2 Electrical activation map

Electrical breakthrough, or the point of the earliest activation, was located in the anterior RV region. Activation time exceeding the mean + 2SD was observed in a total of 19 nodes, and these nodes were within the infarct zone (Figure 8-3B). The electrical activation time was significantly delayed in the infarct zone compared with that of the border zone (31 ± 9 vs. 19 ± 2 msec, $P < 0.05$, Figure 8-4), whereas the electrical activation time was not significantly different between the border zone and the remote zone (19 ± 2 vs. 21 ± 3 msec, $P = \text{n.s.}$).

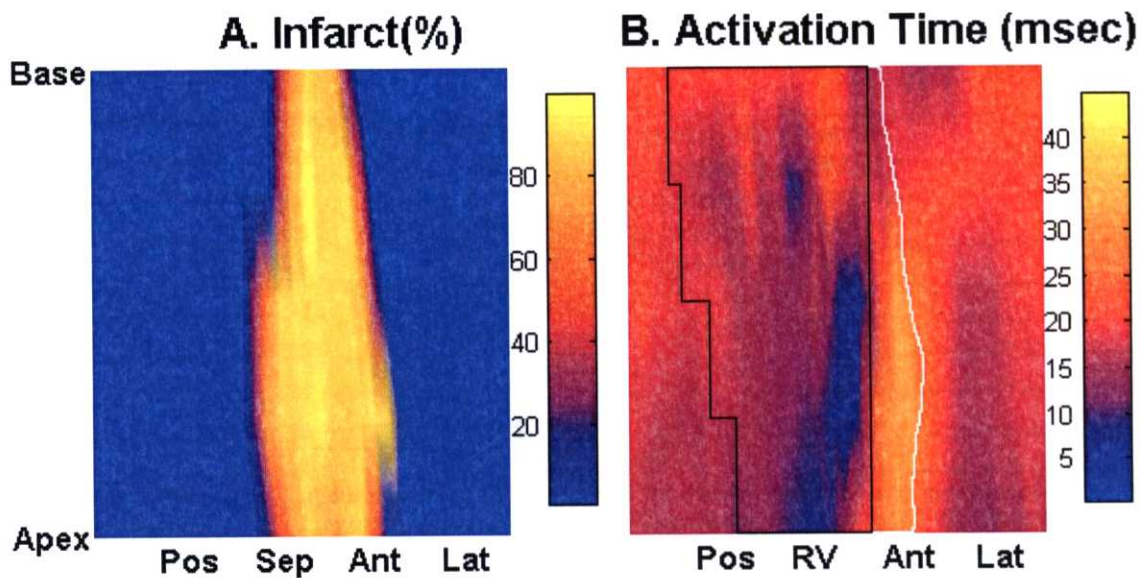


Figure 8-3: Infarct depth and electrical activation from a single animal. A. Infarct map (in percent depth). B. Isochrone map of electrical activation time (in msec). The area circumscribed by a solid black line represents the right ventricle (RV). The area circumscribed by a solid white line represents the infarct zone in the anterior wall (the infarct zone in the septum is covered by the RV). Pos: posterior wall, Sep: septal wall, Ant: anterior wall, Lat: lateral wall.

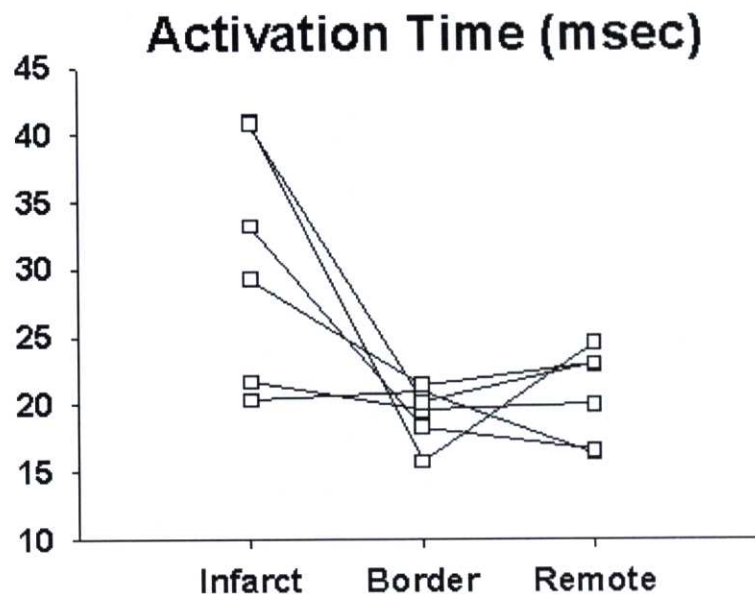


Figure 8-4: Quantitative analysis of electrical activation time in each zone (n=6). Electrical activation time (in msec) was significantly delayed in the infarct zone compared with that of the border zone (31 ± 9 vs. 19 ± 2 msec, $P < 0.05$), whereas it was not significantly different between the border zone and the remote zone (19 ± 2 vs. 21 ± 3 msec, $P = \text{n.s.}$).

8.4.3 Strain map

A 3D displacement map from a single animal is shown in Figure 8-5. Each arrow represents a displacement vector that points from the end-diastolic to end-systolic configuration. The magnitude of displacement is color-coded. It is clear that the displacement magnitude in the infarct zone in the antero-septal wall (left side of the figure) is small (purple ~ blue) compared to that of the remote zone in the posterolateral wall (right side of the figure, red ~ yellow).

The number of strain calculation points was $3,625 \pm 766$ per heart, and each sector contained 11 ± 3 strain points from which average strains were calculated. E_{rr} , E_{cc} and E_{ll} over the infarct zones were smaller in magnitude than those in the remote zones (Figure 8-6). The regions of abnormal strains, particularly the longitudinal strain, extended far beyond the infarct zone, and the strains were larger in the epicardium than in the endocardium.

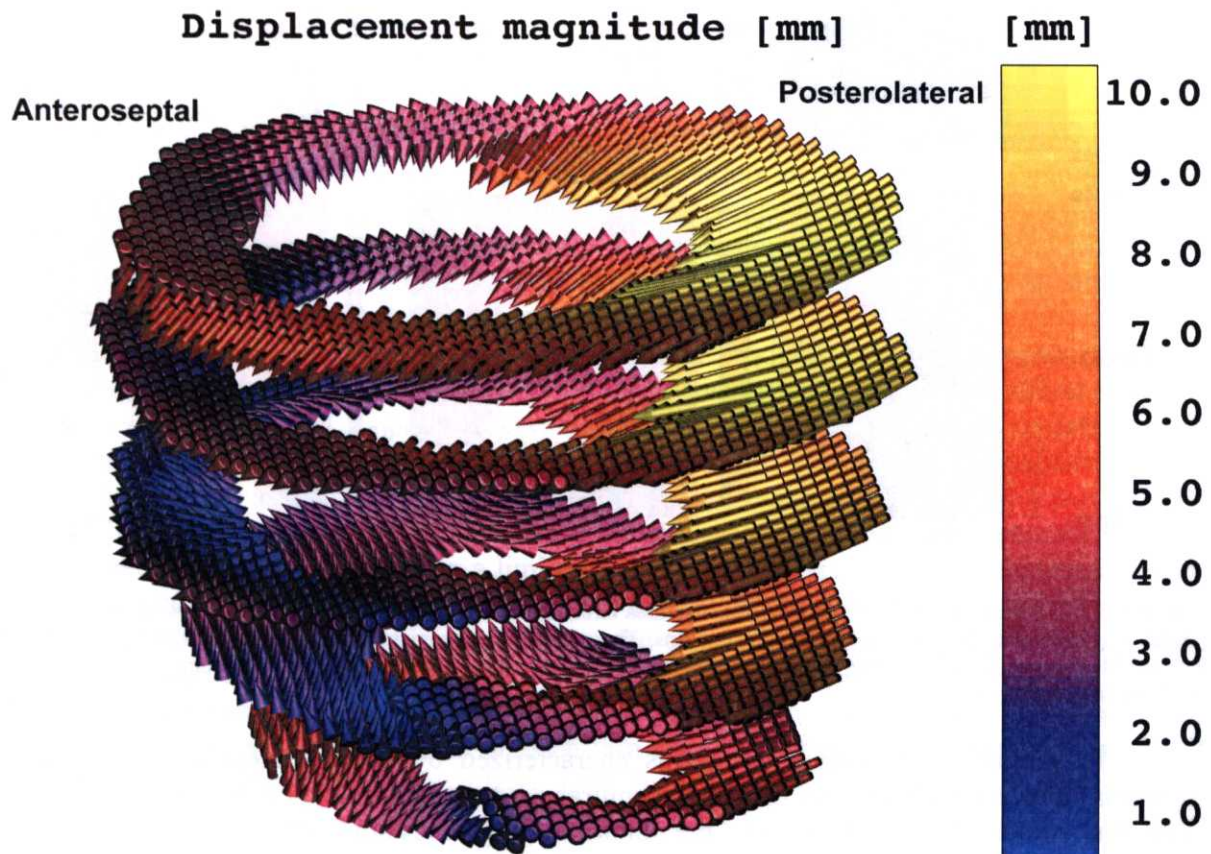


Figure 8-5: 3-D Displacement map from a single animal. Each arrow represents a displacement vector that points from the end-diastolic to end-systolic configuration. The magnitude of displacement is color-coded. It is clear that the displacement magnitude in the infarct zone in the anteroseptal wall (left side of the figure) is small (purple ~ blue) compared to that of the remote zone in the posterolateral wall (right side of the figure, red ~ yellow).

E_{rr} , E_{cc} and E_{ll} in both the infarct zone and the border zone were significantly smaller than those in the remote zone ($P < 0.05$), and there was no significant difference between the infarct zone and the border zone ($P = \text{n.s.}$, Figure 8-7). However, E_{rr} , E_{cc} and E_{ll} in the border zone were more heterogeneous than those in the infarct and remote zones. For example, two animals showed positive circumferential strains in the border zone, which indicate that the myocardium in the border zone underwent a paradoxical systolic stretch in the circumferential direction. Similarly, three animals showed large positive longitudinal strains in the border zone, which suggest that the border myocardium was also stretched in the longitudinal direction during active contraction (Figure 8-7). There was a significant transmural gradient between the epicardium and endocardium in E_{rr} , E_{cc} and E_{ll} in the remote zone ($P < 0.05$), and the transmural gradient was lost in both the infarct zone and the border zone.

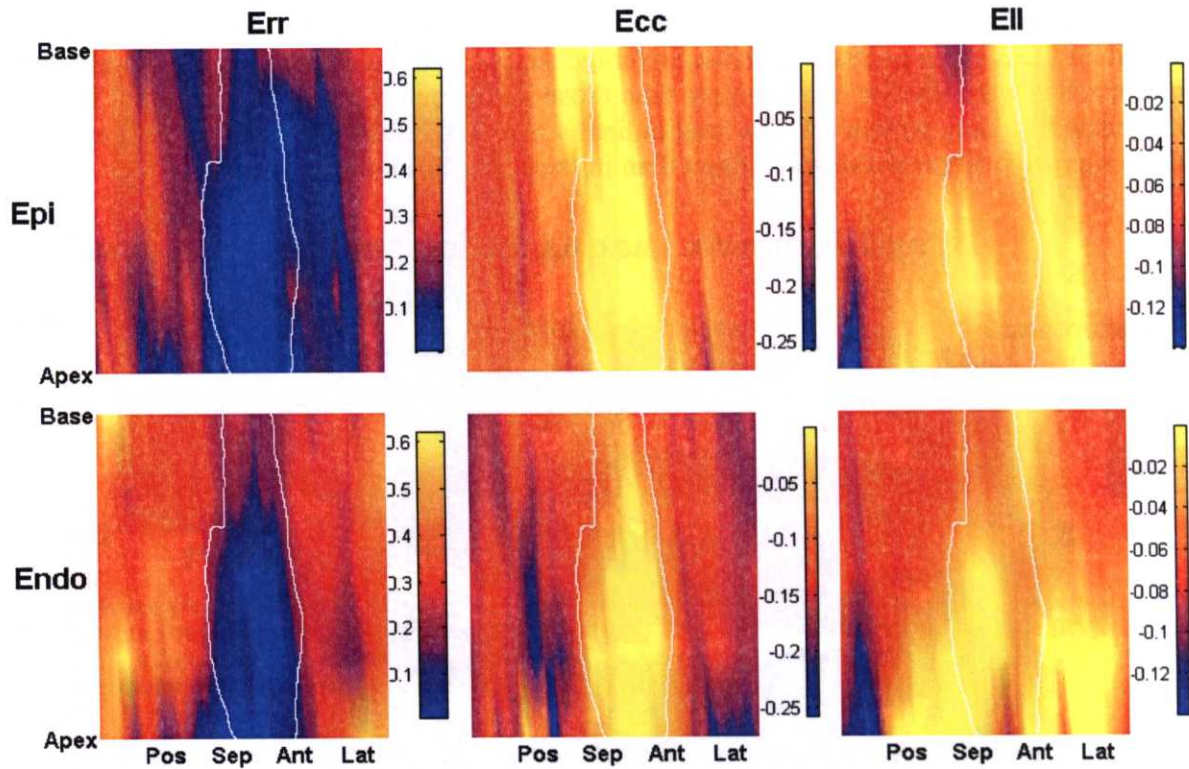


Figure 8-6: 3-D Strain map from a single animal. The area circumscribed by a solid white line represents the infarct zone. E_{rr} : radial, E_{cc} : circumferential, and E_{II} : longitudinal strains. The regions of abnormal strains, particularly the longitudinal strain, extended far beyond the infarct zone, and the strains were larger in the epicardium than in the endocardium. Epi: epicardial layer, Endo: endocardial layer.

In summary, the infarct zone was characterized by delayed electrical activation and abnormal mechanics, including loss of transmural gradient and reduction of strain magnitude or abnormal stretch. In the border zone, the abnormal mechanics similar to that of the infarct zone was observed, however, the electrical activation time was not different from that of the remote zone.

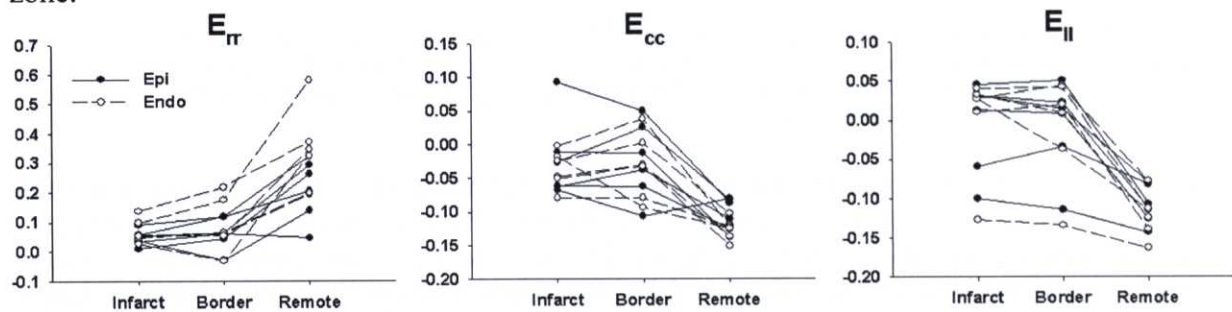


Figure 8-7: Quantitative analysis of finite strain in each zone ($n=6$). E_{rr} , E_{cc} and E_{II} in both the infarct zone and the border zone were significantly smaller than those in the remote zone ($P<0.05$), and there was no significant difference between the infarct zone and the border zone ($P=n.s.$). There was a significant transmural gradient between the epicardium and endocardium in E_{rr} , E_{cc} and E_{II} in the remote zone ($P<0.05$), and the transmural gradient was lost in both the infarct zone and the border zone.

8.5 Discussion

To examine the electrical activation in the infarct border zone with depressed systolic function in chronic MI, the present study combined epicardial electrical recording and high-resolution MR-based imaging techniques to examine the anatomical correlation of local depolarization, myocardial scar, and systolic deformation of the heart.

8.5.1 Impact of infarct geometry on electromechanical properties in the infarct zone

Recent studies have demonstrated that the DHE MRI technique allows accurate assessment of infarct extent and geometry. The spatial extent of DHE was the same as that of myocyte necrosis shown by TTC-stained pathology, independent of wall motion and infarct age (138), and the clinical reproducibility of DHE for determination of infarct size and distribution is highly comparable to that of routine clinical SPECT (160). In addition, DHE is superior to SPECT in detection of subendocardial infarcts (243).

The high-resolution DHE MRI results show that the infarct geometry on the border is highly complex (Figure 8-2). The infarct was mostly non-transmural, and the infarct size was approximately 30% of the LV, both observations are consistent with previous reports using a similar occlusion-reperfusion infarct model in canine (78, 95, 96, 129, 248). Traditionally, the infarct zone has been associated with delayed electrical activation and slow conduction velocity (69, 78, 97, 235). As a result of the relatively small size and nontransmural geometry of the infarct, delayed electrical activation in a limited region of the infarct zone was observed (Figure 8-3). The nontransmural geometry of the infarct in this model is not only due to reperfusion, but also due to rich collateral circulation intrinsic to the canine heart, as compared to humans and other species such as swine. Permanent coronary ligation in swine tends to result in a well-demarcated, transmural scar, whereas the canine MI model in the present study is characterized by a relatively large volume of viable myocardium over the infarct zone. Holmes *et al.* (115) studied systolic deformation of the infarct zone in a small region in the LV free wall by permanent occlusion of obtuse marginal branches of LCx in swine. Despite impaired systolic shortening, they found significant systolic wall thickening (E_{π}) still present at 3 weeks, which is suggestive of passive deformation in the regions composed almost entirely of collagen (114). In contrast, the results indicate significant impairment of systolic deformation and loss of transmural gradient in E_{π} , E_{cc} and E_{ll} including systolic wall thickening in the infarct zone (Figure 8-4A and 8-5B). Therefore, the difference in the infarct geometry appears to account for distinct characteristics in mechanics as well as electrical activation.

8.5.2 Mechanism of impaired systolic function in the infarct border zone

It was hypothesized that impaired systolic function in the infarct border zone may be partially accounted for by delayed electrical activation. However, the electrical activation in the infarct border zone was not delayed compared with that of the remote zone (Figure 8-3 and 8-4), whereas the systolic function of the border zone was depressed relative to that of the remote zone (Figure 8-6 and 8-7). These findings indicate that electrical factors do not contribute to the impaired systolic function in the border zone, but the border zone dysfunction most likely results from mechanical interaction between the ischemic and normal myocardium. Although the details of this interaction are not fully understood, mechanical ‘tethering’ due to high wall stress appears to be a predominant mechanism (93, 94, 156, 163, 210, 238). Besides, recent studies have demonstrated that the LV myocardial shortening is regionally heterogeneous (271), and the timing and the peak of shortening may be controlled by nonuniform prestretch from atrial

contraction via a regional Frank-Starling effect (272). Although prestretch during atrial contraction in the border zone was not quantified because the time course of finite strain was not examined, it is speculated that a higher wall stress in the border zone may lead to a smaller diastolic prestretch, which may contribute to generating delayed and little shortening.

Of note, the high-resolution motion tracking MRI revealed a paradoxical systolic stretch (eccentric contraction) in the border zone of some animals (Figure 8-7). This systolic stretch is clinically important because it may generate a stretch-activated ectopy to trigger reentry ventricular arrhythmia in patients with ischemic heart. Whether the border zone undergoes little shortening (isometric contraction) or stretch is most likely determined by the loading conditions, the local material property during ventricular tension development, and the ventricular geometry which dynamically changes as structural remodeling progresses. Anatomy-based description of mechanics in the myofiber direction may identify the geometrical and hemodynamic factors that contribute to systolic stretch in the border zone.

8.5.3 Limitations

In the present study, the 3D finite deformation of the LV wall was examined in open-chest, anesthetized dogs. Therefore, the results may not precisely reflect the cardiac mechanics in closed-chest, awake animals. The spatial registration error in this electromechanical mapping technique has been previously reported to be 2.1mm on average, with a precision of marker localization in the images and on the excised heart of 1.0 and 0.7mm, respectively (88). The temporal resolution of electrical activation was 1ms, and this means that the temporal error was within approximately one sample point (≈ 1 ms). Although this mapping technique assumes that the heart be undeformed between the *in situ* and excised states without controlled perfusion fixation *in situ*, previous studies have reported high precision in registering electrode locations over the epicardial surface (88). Due to MR compatibility issues, the electrical mapping in this study was limited to the epicardium. At present, commercially available basket catheters contain ferromagnetic material and would severely degrade image quality. Clinical applicability of this technique to the study of cardiac electromechanics may be limited by surgical intervention and mechanical restriction from the sock. Due to a highly elastic property of the sock material, its mechanical restriction on the heart was minimal, although this effect has not yet been quantified.

8.6 Conclusions

Using a high-resolution electromechanical mapping system, it was demonstrated that abnormal electrical activation is observed in a limited region in the infarct zone, whereas the region of abnormal mechanics extends far beyond the infarct zone in chronic MI. The infarct border zone is characterized by abnormal mechanics directly coupled with normal electrical depolarization. These findings indicate that electrical factors do not contribute to the impaired systolic function in the border zone, but the border zone dysfunction most likely results from mechanical interaction between the ischemic and normal myocardium.

Chapter 9

Global electromechanics in infarct heart with substrate for sudden cardiac death

9.1 Abstract

Alteration of action potential duration (APD) induced by abnormal myocardial stretch (“prestretch”) may increase the risk for sudden cardiac death (SCD) in chronic myocardial infarction (MI) by increasing the dispersion of repolarization and thus susceptibility to ventricular tachyarrhythmia. However, the effect of prestretch on APD in chronic MI *in vivo* has not been quantitatively characterized. The anatomical correlation between prestretch and activation recovery intervals (ARI) was examined in a swine model of chronic MI *in vivo* where sustained monomorphic ventricular tachycardia is inducible with programmed stimulation. Four weeks after anteroseptal MI was created (n=8), high temporal resolution (9msec) tissue-tracking MRI was used to characterize prestretch, and a 247-lead epicardial sock was subsequently placed over the ventricular epicardium to measure ARI under thoracotomy. Prestretch appeared in early systole (30msec), peaked at 70-100msec and persisted until 240-260msec. Prestretch was highest in the posterolateral viable region opposite to the MI ($10.8 \pm 7.4\%$), and lowest in the septal region ($0.4 \pm 0.2\%$) ($P < 0.05$). Prestretch significantly correlated with peak shortening rate ($P < 0.001$). The magnitude of prestretch was similar in the viable and infarct myocardium, but the mechanical function in the infarct myocardium was significantly depressed. There was a strong and consistent correlation between prestretch and ARI in all animals ($P < 0.001$). In conclusion, prestretch in chronic MI prolongs local ARI in a magnitude-dependent manner in swine with a substrate for SCD. Early interventions to reduce prestretch may help reduce SCD in patients with chronic MI.

9.2 Introduction

Recent prospective multicenter clinical trials demonstrate a major survival benefit with the implantable cardioverter-defibrillator (ICD) for sudden cardiac death (SCD) in high-risk subgroups with LV dysfunction due to prior myocardial infarction (MI) and nonischemic cardiomyopathy (149). However, these high-risk subgroups constitute only a small fraction of all the SCDs, thus interventions in these subgroups do not have a major impact on the general public health problem of SCD (183). The majority of the potential SCD victims are not protected by the current guidelines, primarily due to lack of specific markers with high predictive value (269).

SCD mainly results from ventricular tachyarrhythmia (30), thus is an electrical phenomenon. Inducibility of sustained monomorphic ventricular tachycardia (VT) during the invasive electrophysiological study with programmed electrical stimulation (PES) is clinically equivalent to having an arrhythmic substrate, thus has been used as a prognosticator for subsequent mortality (47). However, its prognostic accuracy is relatively low (47, 48, 70). Moreover, its invasive nature does not warrant its use in the “unprotected” yet low-risk subgroups.

Recent studies demonstrate that the mechanical and electrical phenomena in cardiomyocytes are interdependent (146). For example, mechanical myocardial stretch alters action potential duration (APD) (204). Because myocardial scar and structural remodeling confer significant heterogeneity to the material properties of the LV, the regions of greater compliance that experience abnormal stretch, or “prestretch”, may have altered APD (170), which may increase the dispersion of repolarization within the ventricles and thus the susceptibility to ventricular tachyarrhythmia (27, 91, 204). In fact, strategies to suppress prestretch in patients with LV dysfunction have consistently proven to be successful. For example, beta-blockers, which likely diminish prestretch due to the negative inotropic effect, reduce mortality among patients with heart failure due to a significant reduction in fatal arrhythmias (59). Furthermore,

cardiac resynchronization therapy (CRT) aims to cancel the prestretch in the lateral LV by electrically stimulating the region of prestretch, and improves morbidity and mortality in patients with intraventricular conduction delay (40, 58)

Stretch is a mechanical phenomenon, thus can be noninvasively quantified with MRI (194). Quantitative characterization of the effect of prestretch on APD may establish the link between the mechanical and electrical phenomena in the heart *in vivo*, and allow an MR-guided, noninvasive risk assessment of SCD in these “unprotected” subgroups. The hypothesis of this work is that the prestretch in chronic MI with a substrate for SCD alters the local APD *in vivo*. To test this hypothesis, the anatomical correlation between prestretch and activation recovery intervals (ARI) in a swine model of chronic MI was quantitatively examined where sustained monomorphic VT is inducible with PES. A high-resolution cardiac electromechanical mapping technique (88) allowed acquisition of anatomical, electrical, and mechanical data with high precision.

9.3 Materials and Methods

All studies were performed according to the *Position of the American Heart Association on Research Animal Use* (2). All animal protocols were reviewed and approved by the Animal Care and Use Committee of the National Heart, Lung and Blood Institute, which is accredited by the American Association for Accreditation of Laboratory Animal Care.

9.3.1 Creation of myocardial infarction

Eight domestic swine (34–47kg) were anesthetized with intravenous sodium thiopental (10-20mg/kg), intubated, and mechanically ventilated with a mixture of oxygen, medical air and isoflurane (1-3%). The surface ECG and the arterial pressure were recorded throughout the procedure. A modified version of a catheter-based MI procedure was used that has been described previously (213). Briefly, a balloon angioplasty catheter (2.7Fr) was advanced to the middle portion of LAD through a 6Fr guiding catheter via a carotid artery. The balloon was then inflated to 6atm to occlude LAD, and the occlusion was maintained for 150min. After completion of balloon occlusion, the catheters were removed, the surgical wound closed, and the animals extubated and recovered.

9.3.2 *In vivo* MRI

Four weeks after MI, the animals were anesthetized as above to undergo *in vivo* MRI in a 1.5T scanner (Espree, Siemens) with an 8-channel surface coil (Figure 9-1B). LV geometry (end-diastolic and end-systolic volumes) and global function (stroke volume and ejection fraction) were evaluated with a cine steady state free precession (SSFP) sequence (bandwidth (BW) $\pm 930\text{Hz/pixel}$, echo time (TE) 1.78msec, repetition time (TR) 3.56msec, readout flip angle 35° , FOV $233 \times 311\text{mm}$, image matrix 192×256 , spatial resolution $1.2 \times 1.2 \times 8.0\text{mm}$, 6 slices). LV regional function was evaluated with a 2-D myocardial tissue tracking sequence (137) (cine-DENSE, BW $\pm 1,008\text{Hz/pixel}$, TE/TR 4.52/9.0msec, readout flip angle $12\text{--}20^\circ$, FOV $400 \times 200\text{mm}$, image matrix 128×64 , spatial resolution $3.1 \times 3.1 \times 8.0\text{mm}$, 6 slices). The slice positions and the orientations of the cine-DENSE images were set to the same as those of the cine SSFP images to facilitate registration processes. A total of 45-65 images were acquired through systole with temporal resolution 9.0msec. LV short-axis image slices from LV base to apex were acquired in a consistent manner based on predetermined anatomical landmarks without gaps between slices. Each image acquisition was ECG-gated, and the image was acquired during a single breath hold (40–60sec) by manually holding mechanical ventilation at end-expiration.

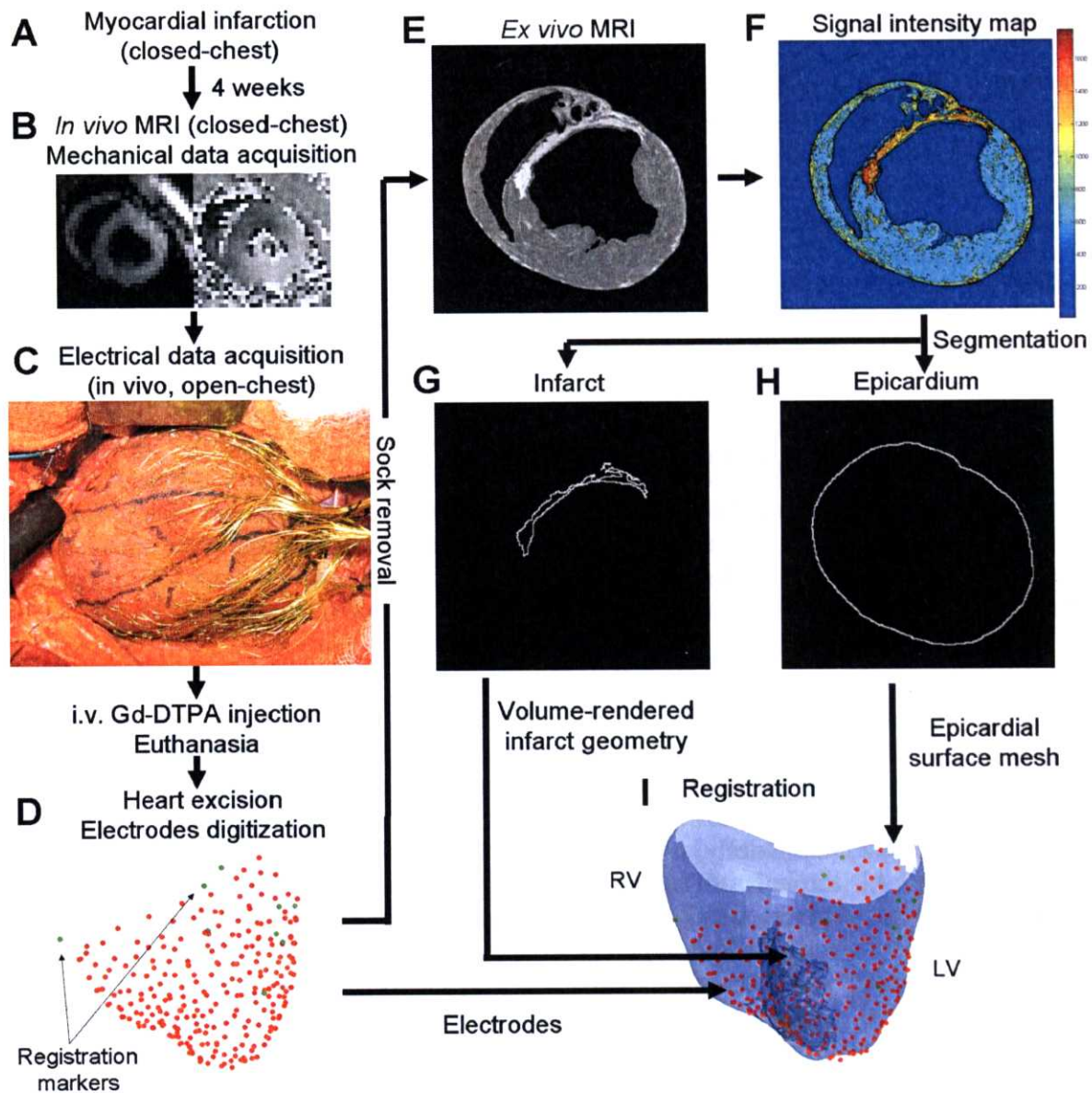


Figure 9-1: Overview of data acquisition and processing.

9.3.3 Electrical recording system

After MRI, the animals were transported to the operating room and underwent median sternotomy. A multi-electrode epicardial sock, consisting of a nylon mesh fitted with 247 silver electrodes (electrode spacing = 2-5mm) attached in an ordered fashion, was placed over the ventricular epicardium (Figure 9-1C) (19). The sock was placed in a consistent and predetermined orientation and secured with several sutures. A ground reference electrode was sewn onto the fat pad at the aortic root. Electrical signals from the 247 electrodes were amplified (gain=1,000) and were acquired using a 16-bit analog-to-digital converter (PXI-6225x4, National Instruments) at a minimum sampling rate of 1,000Hz for 10sec (29). Electrical recording was conducted during normal sinus rhythm and sustained monomorphic ventricular tachycardia (VT).

9.3.4 Induction of monomorphic ventricular tachycardia

A pair of bipolar stimulating wires was directly attached to the RV outflow tract (RVOT) using an alligator clip, and a modified version of a swine PES protocol (213) was conducted to test the inducibility of sustained monomorphic VT. Briefly, following regular ventricular pacing (S1) at a cycle length of 250, 300 and 350 msec, single (S2), double (S2, S3), or triple (S2, S3, S4) premature stimuli were introduced with a pulse width of 2msec. The endpoints of the protocol were (1) completion of the protocol without inducing VT or ventricular fibrillation (VF); or (2) induction of two episodes of sustained monomorphic VT or VF. Sustained VT was defined as monomorphic VT lasting more than 15sec, and was confirmed in multiple leads. VT or VF was electrically defibrillated using an internal defibrillation pads, and the cables to the electrical recording system were temporarily disconnected before defibrillation to protect the system. When either endpoint was reached, the stimulating protocol was completed.

9.3.5 Postmortem studies

Upon completion of PES, heparin 5,000IU and Gd-DTPA 0.20mmol/kg were administered intravenously and the animals euthanized 15-20min after Gd-DTPA. The heart was removed, and was filled with vinyl polysiloxane, maintaining end-diastolic shape (88). As markers for registering the MR and the sock data, eight to fifteen 10mm x 1mm glass tubes filled with Gd-DTPA (5 mM) were placed in the myocardium, and the locations of the sock electrodes and the glass tubes were digitized (Microscribe 3DLX, Immersion, San Jose, CA) (Figure 9-1D) (88). The sock electrodes were removed from the heart. To evaluate the extent of MI with high spatial resolution, ex vivo contrast-enhanced MR imaging(109) was performed in the 1.5-T MR scanner. A 3D Gradient recalled echo (GRE) sequence was used to visualize MI and to locate the glass tube markers (BW \pm 170Hz/pixel, flip angle 20°, TE/TR 3.71/9.28msec, FOV 120x120x100mm, image matrix 256x256x192, spatial resolution 0.5mmx0.5mmx0.5mm) (Figure 10-1E).

9.3.6 Data processing

Custom programs in MATLAB (Mathworks, Inc.) and C⁺⁺ were used for data analysis. The infarct geometry was extracted from the 3D GRE images using a signal intensity threshold to visualize a volumetric image of infarct in the ventricles (Figure 9-1F) (18). The MI was segmented as the hyperenhanced region that was seen in >1slice in the 3D GRE images. The hyperenhanced region was defined as >6 standard deviation (SD) of the signal intensity above the mean intensity of the circular region (diameter ~10mm) in the remote, viable myocardium (Figure 9-1G) (186). The values of the MI depth at the cine-DENSE image slice positions were determined using bicubic interpolation (19). The ventricular epicardial surface was extracted from the MR images, and the spherical harmonic mesh (117) was created to subsequently visualize electrical data (Figure 9-1H). The locations of the glass tube markers were determined from the MR images, and the electrodes were spatially referenced to the MR images using rigid-body transformation (Figure 9-1I) (88).

The local activation recovery interval (ARI) was measured between times of electrical activation ($=dV/dt_{\min}$ of the QRS) and recovery. Electrical recovery was defined as the dV/dt_{\max} of the T wave for negative T wave, the dV/dt_{\min} of the T wave for positive T wave, and at the mean time between dV/dt_{\max} and dV/dt_{\min} for biphasic T wave (259). ARI between electrodes was calculated using bicubic interpolation.

The LV endocardial border was manually segmented in the LV short-axis cine SSFP images to calculate global LV function using MIPAV (NIH) (164). The cine-DENSE sequence

used for tissue-tracking encodes one-dimensional (1-D) displacement of each pixel from the reference time point as stimulated echoes in the phase image (Figure 9-2) (4).

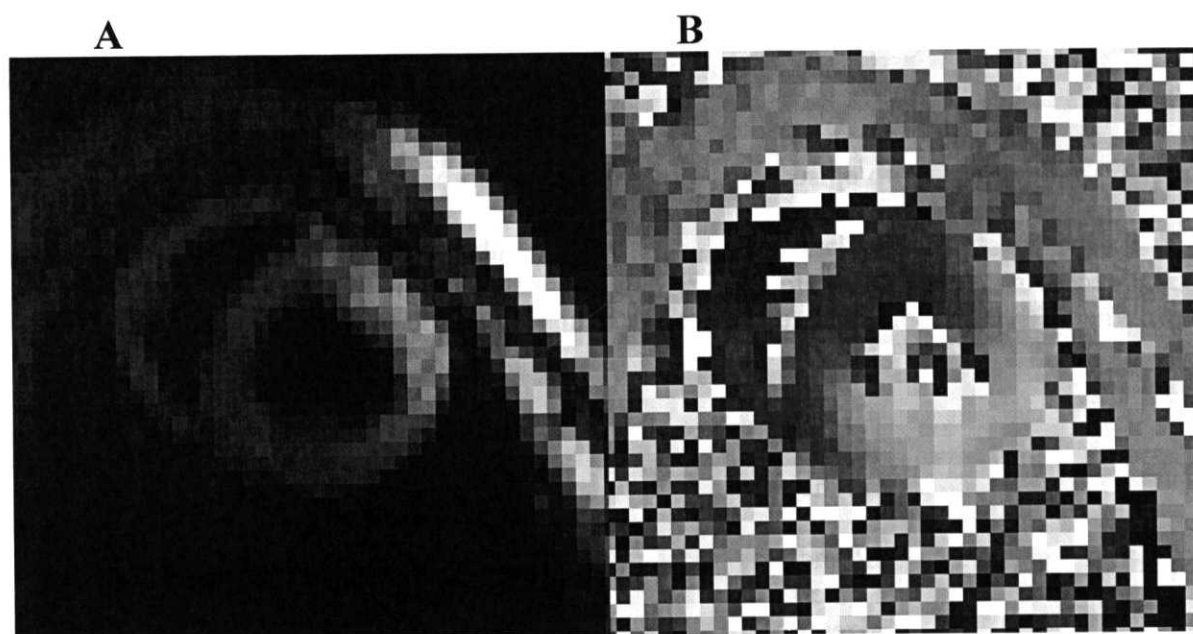


Figure 9-2: The magnitude (A) and the phase (B) images from the cine-DENSE sequence.

A previously published protocol of image acquisition, displacement and strain calculation was followed (137). Briefly, two separate image acquisitions were performed consecutively to obtain 1-D displacement information in two orthogonal directions (Figure 9-3).

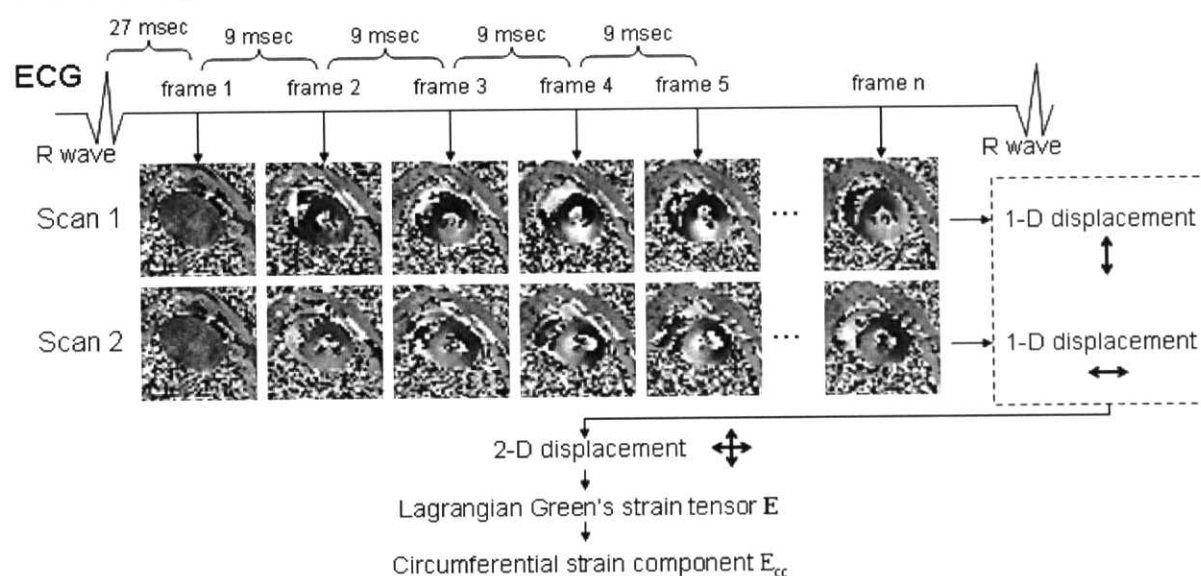


Figure 9-3: Image acquisition, displacement and strain calculation using the cine-DENSE sequence.

The LV myocardium was manually segmented and the 2-D phase information in each pixel was unwrapped and was converted to 1-D displacement. The 2-D displacement of each pixel was computed by means of vector addition of the two orthogonal 1-D displacement. Regional Lagrangian Green's strain tensor \mathbf{E} was computed by means of isoparametric

formulation with quadrilateral elements (175). Each quadrilateral element was a square 4-pixel neighborhood of myocardium where the final position of each element of myocardium is known (the pixel location), and the initial 2D position of each pixel is measured. After diagonalization of \mathbf{E} , the directions of the first and second principal strains and the corresponding eigenvalues were found. Relative to the center of mass of the left ventricle, the circumferential strain component E_{cc} were computed by means of projection of \mathbf{E} into the circumferential directions.

The circumferential strain ϵ_c (Figure 9-4A) was calculated from the Lagrangian Green's strain tensor as the percent change in length of a small line segment in the circumferential direction (272):

$$\epsilon_c = (\sqrt{1 + 2E_{cc}} - 1) \times 100\%$$

where E_{cc} is the Lagrangian Green's strain component in the circumferential direction. By convention in continuum mechanics, a negative strain represents shortening (e.g. -15%), whereas a positive strain represents stretch (e.g. +15%) in the circumferential direction.

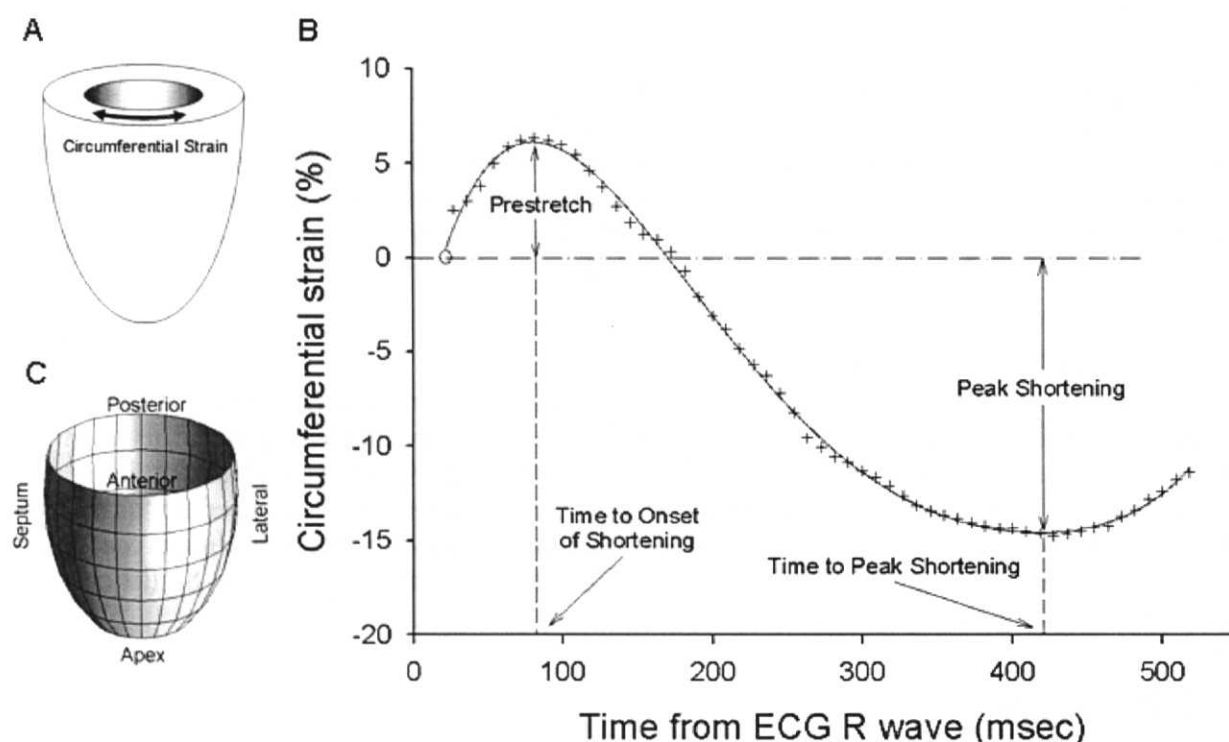


Figure 9-4: *A. Circumferential strain.* Circumferential strain ϵ_c describes myocardial shortening or stretch in the circumferential direction. *B. Sample fit of raw circumferential strain data at imaging times (+) to 7th-order polynomials (solid line).* Prestretch was defined as the maximum strain (=stretch) prior to systolic shortening, and the onset of shortening was defined as the time of prestretch. Peak shortening was defined as the minimum strain (=shortening) before diastolic stretch. *C. Mesh reconstruction of LV.* Mesh vertices indicate locations of displacement and strain calculations. There are a total of 144 data points per heart (=24 sectors x 6 short-axis slices).

The short-axis LV circumference was divided into 24 sectors, and the average circumferential strain in each sector was calculated. The reference configuration (strain=0%) was defined at the time of the tag encoding gradient, which occurred at 22msec after the peak R wave, and the first cine-DENSE image took place at 27msec after the peak R wave. The strains were interpolated across time using a seventh-order polynomial fit to all of the data points (Figure 9-

4B). The seventh-order polynomial was chosen over other orders of polynomial fits and local cubic splines because it provided a good trade-off between accuracy of the fit and noise reduction of the data (252).

Abnormal stretch, or “prestretch”, was defined as the maximum strain (= stretch) prior to systolic shortening, and peak prestretch rate was defined as the positive peak of the time derivative of the circumferential strains during prestretch. The onset of shortening was defined as the time of prestretch, and peak shortening was defined as the minimum strain (=shortening) before diastolic stretch. Peak shortening rate was defined as the negative peak of the time derivative of the circumferential strains during shortening. Strain data in sectors where prestretch or peak shortening was not observed were excluded from analysis.

Each LV had 144 mechanical data points (= 24 sectors x 6 short-axis slices), and a 3-D prolate ellipsoid mesh described by Bovendeerd *et al* (38) was used to present the data (Figure 9-4C). A bicubic surface through existing data points were fitted to the mechanical data, where the value of an interpolated point is a combination of the values of the sixteen closest points. The circumferential length of each sector in the figures was shortened or lengthened based on ϵ_c to visually demonstrate the dynamic motion of the LV with reference to the undeformed configuration.

9.3.7 Electromechanical data registration

To evaluate the correlation between electrical and mechanical indices involved in prestretch, electrical data were analyzed in the regions of prestretch. The electrical data in the LV was spatially referenced to mechanical data based on pre-determined anatomical landmarks. A bicubic surface fit was used to calculate the electrical indices at the mechanical data points in the LV that was covered by the epicardial sock electrodes.

9.3.8 Statistical analysis

Values are means \pm SD (n=8). One-way analysis of variance (ANOVA) was used to compare maximum and minimum mechanical indices, and mechanical indices between the viable and infarct myocardium. If a statistically significant result was obtained, individual locations were compared by a two-tailed *t* test. Linear regression was used to assess the correlation between prestretch and other indices, and expressed with their correlation coefficient (*r*) and *P* value. A value of *P*<0.05 was considered statistically significant. Statistics were performed with SigmaStat 3.0 (SPSS, Chicago, IL).

9.4 Results

9.4.1 General parameters

All animals survived the infarct procedure, which resulted in anteroseptal MI (Figure 9-5). The animals underwent MR studies and VT induction 29 \pm 5days after MI. Sustained monomorphic VT was induced in all animals, which indicate that all animals had a substrate for ventricular tachycarrhythmia (Figure 9-6). All induced VTs were hemodynamically unstable, likely due to relatively short cycle length (CL) (133 \pm 22 msec). Hemodynamic parameters during the MRI study are summarized in Table 9-1. The time course of circumferential strain by tissue-tracking MRI covered 86 \pm 21% of cardiac cycle (Table 9-2). The heart rate during the open-chest electrical measurements was 129 \pm 13bpm, and this value was significantly larger than that of the *in vivo* MRI study (97 \pm 28bpm, *P*=0.019).

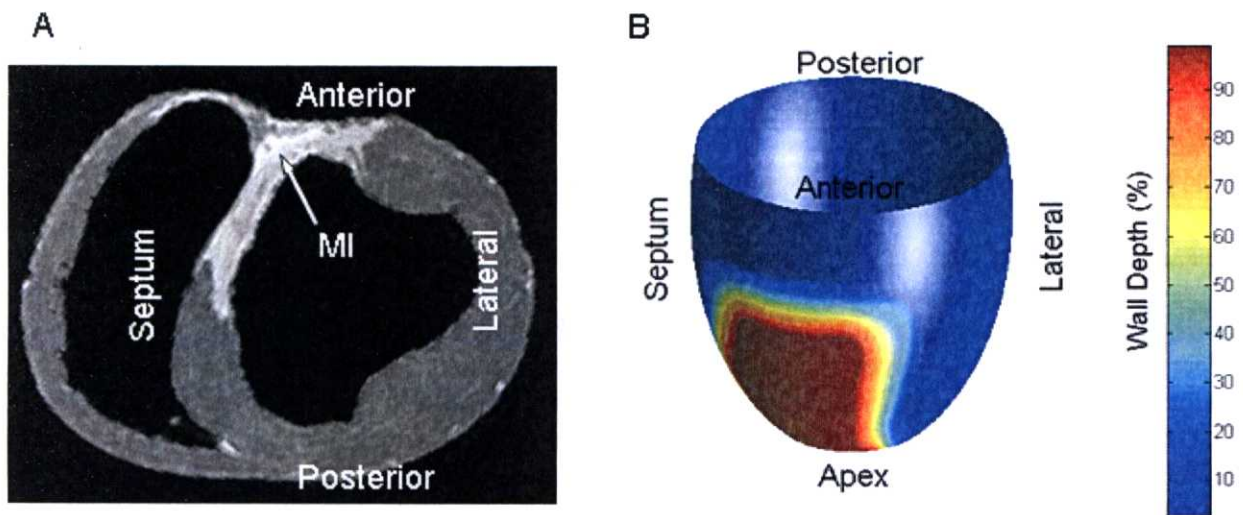


Figure 9-5: A. Short-axis view of the contrast-enhanced MR image. Regions of high intensity (= light gray) corresponds to MI. B. Mesh presentation of the MI wall depth (%) in one animal. Note the MI was mostly transmural (= dark red), and was located in the anteroseptal region.

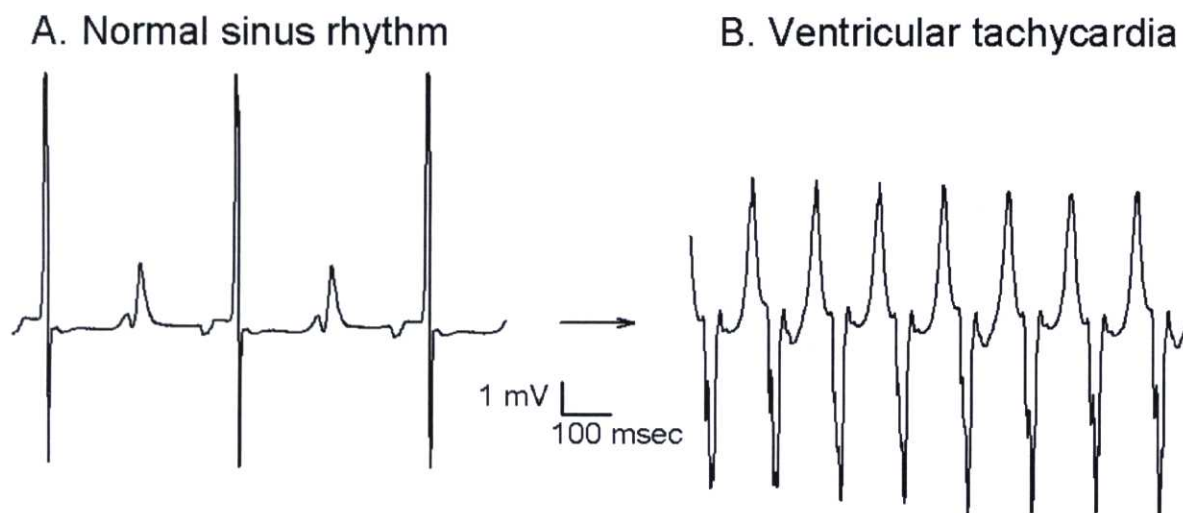


Figure 9-6: Unipolar electrical recordings from an epicardial sock electrode. A. Normal sinus rhythm, B. Sustained monomorphic VT.

Parameters	Mean \pm SD (n=8)
Heart rate (bpm)	96.8 \pm 28.4
LV end-diastolic volume (mL)	59.7 \pm 8.7
LV end-systolic volume (mL)	36.5 \pm 5.3
LV ejection fraction (%)	38.7 \pm 4.7
Stroke volume (mL)	23.2 \pm 4.7
Cardiac output (mL/min)	2,205 \pm 708.2

Table 9-1: Hemodynamic parameters at the time of MRI studies.

Parameters	Mean \pm SD (n=8)
Cycle length (msec)	669 \pm 198
Cine-DENSE coverage (msec)	546 \pm 92
Time coverage per cardiac cycle (%)	86 \pm 21

Table 9-2: Time coverage by cine-DENSE sequence per cardiac cycle.

9.4.2 Infarct geometry

The MI was mostly transmural due to little collateral circulation intrinsic to the swine heart, and was non-transmural only at its anterior and septal edges (Figure 9-5A). On the anterior edge, the MI usually involved the anterior segment of the anterolateral papillary muscle on the endocardial border. The MI also expanded to the anterior portion of the right ventricle (RV). The myocardial wall in all portions of the MI exhibited substantial thinning. The mesh presentation of the MI wall depth (%) in one animal is shown in Figure 10-5B. On average, the MI covered 23 \pm 4% of the LV surface (n=8).

9.4.3 Characteristics of prestretch

Figure 9-7 shows circumferential strains over time in the mesh representation of the LV in one animal during normal sinus rhythm. The time course of mechanical mapping showed substantial heterogeneity in strain distribution. The viable myocardial tissue that occupied the majority of the LV underwent normal systolic deformation sequence, shown in light green (0%), cyan (-5%), blue (-10%), then dark blue (-15%). In contrast, the MI region (circumscribed by a solid line) underwent substantial systolic stretch, shown in yellow (5%) as viable myocardium shortens (blue). The viable myocardium in the lateral region exhibited significant prestretch (yellow-red) during early systole. Significant prestretch (red) appeared around 30msec in the lateral, viable myocardium when the majority of the LV has not started contraction yet (light green). Prestretch peaked at 70-100msec, and persisted until 240-260msec. Regional heterogeneity of prestretch-related mechanical indices is shown in Figure 10-8 and Table 9-3. Comparison of mechanical indices between the viable vs. infarct myocardium is summarized in Figure 9-9.

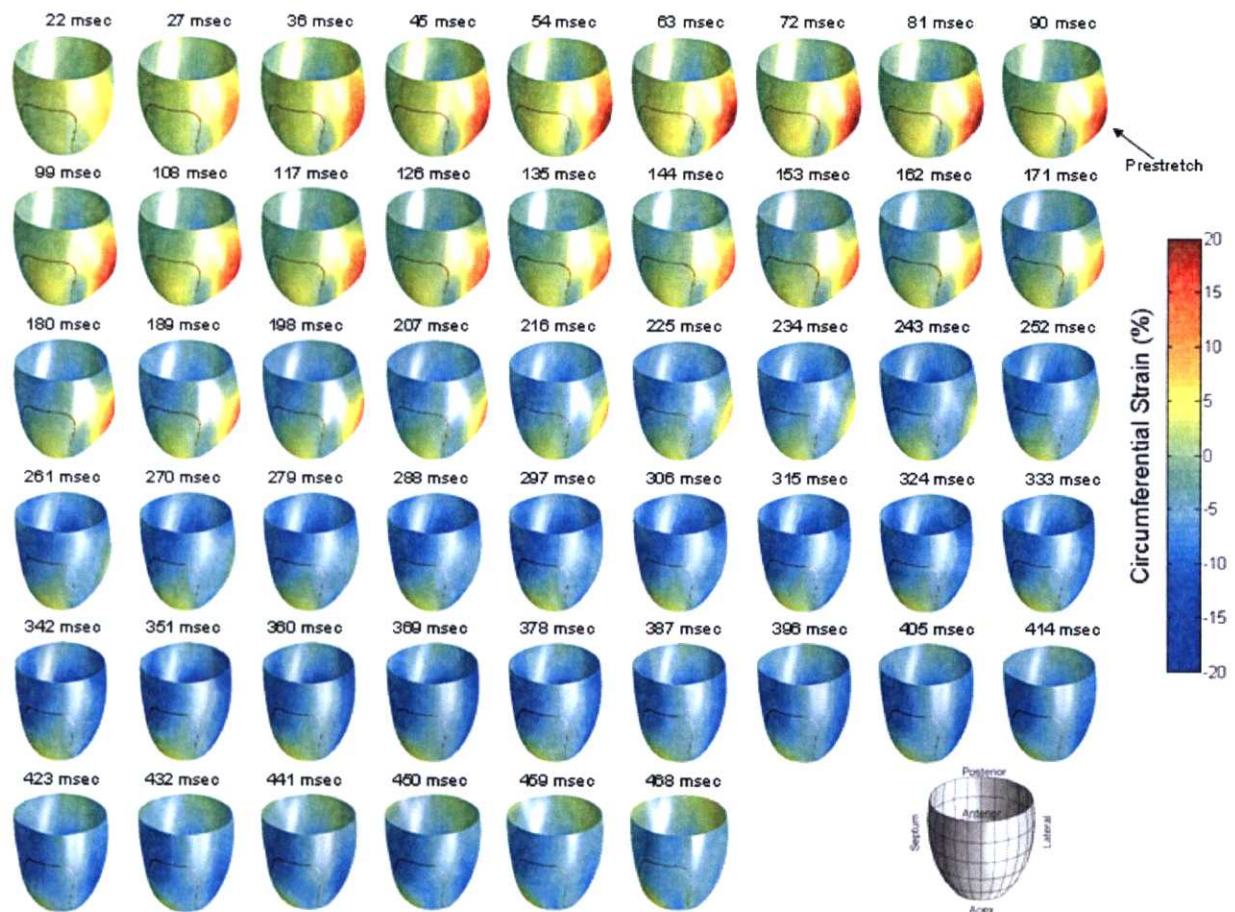


Figure 9-7: Time course of circumferential strain in one animal. Note that prestretch (shown in yellow-red) appears at around 30msec in the lateral region when the majority of the LV myocardium has not started contraction yet (shown in light green). Prestretch peaked at 70-100msec, and persisted until 240-260msec. The area circumscribed by a solid line represents MI (>50% wall depth). Note the circumferential length change appears greater than actual change *in vivo*.

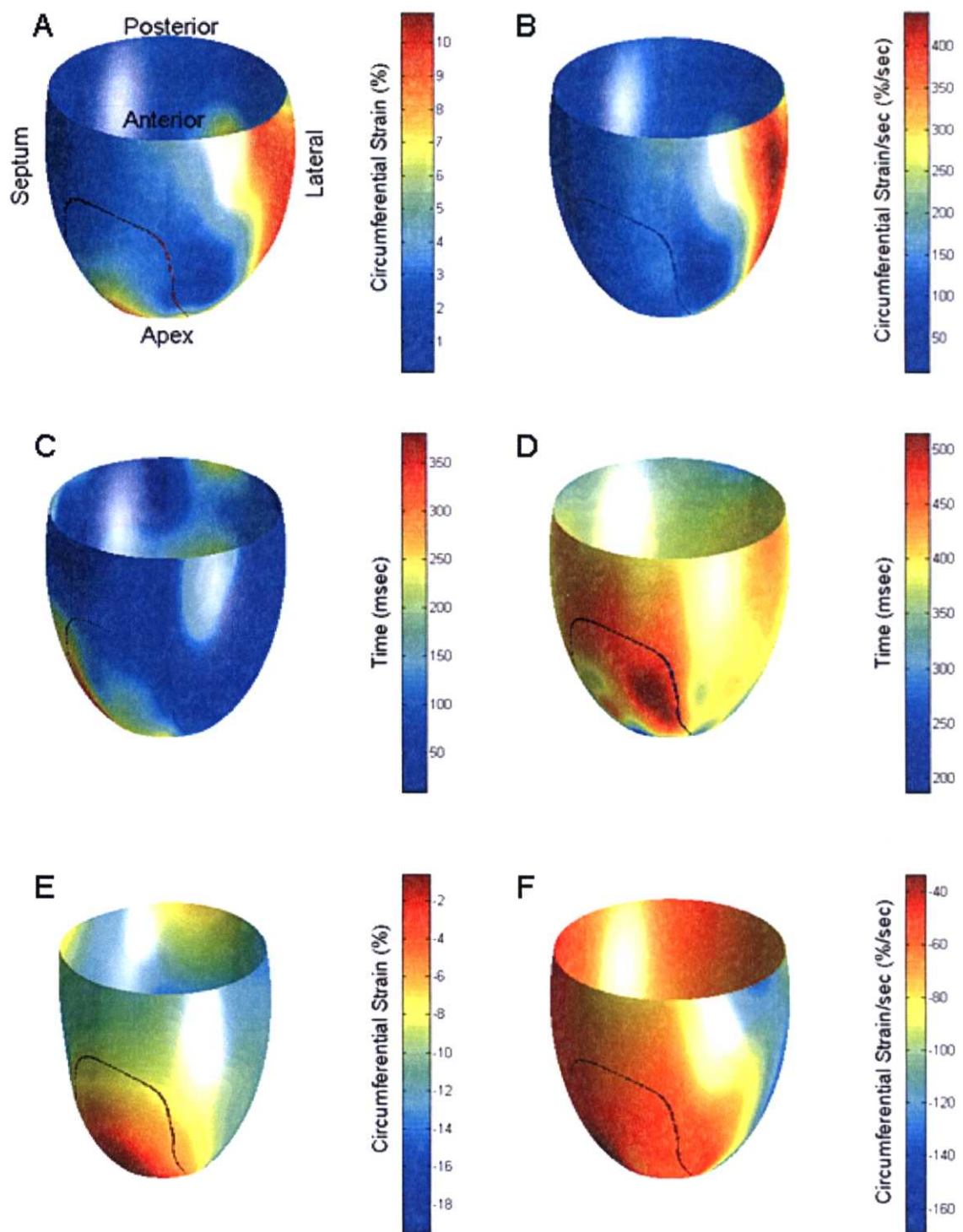


Figure 9-8: *Average mechanical indices by region (n=8)*. A. Prestretch (circumferential strain, %), B. Peak prestretch rate (circumferential strain/sec, %/sec), C. Time to onset of shortening (time, msec), D. Time to peak shortening (time, msec), E. Peak shortening (circumferential strain, %), F. Peak shortening rate (circumferential strain/sec, %/sec). The area circumscribed by a solid line represents MI (> 50% wall depth).

Parameters	Average	Minimum	Maximum
Prestretch (%)	4.6 ± 5.3	0.4 ± 0.2	10.8 ± 7.4*
		Septal (viable)	Posterolateral (viable)
Peak prestretch rate (%/sec)	176.3 ± 199.0	7.1 ± 3.3	442.3 ± 324.6*
		Septal (viable)	Lateral (viable)
Time to onset of shortening (msec)	112.7 ± 150.4	34.2 ± 10.1	392.9 ± 310.4*
		Posterolateral (viable)	Anteroseptal (MI)
Time to peak shortening (msec)	392.3 ± 91.4	199.9 ± 299.1	523.1 ± 79.0*
		Septal (viable)	Anteroseptal (MI)
Peak shortening (%)	-11.3 ± 4.7	-19.6 ± 4.5	-0.7 ± 1.3*
		Posterolateral (viable)	Anteroseptal (MI)
Peak shortening rate (%/sec)	-80.0 ± 43.9	-170.5 ± 91.7	-33.6 ± 12.0*
		Lateral (viable)	Anteroseptal (MI)

Table 9-3: *Minimum vs. maximum mechanical indices by region.* Values are means±SD (n=8). *: P<0.05 vs. Minimum.

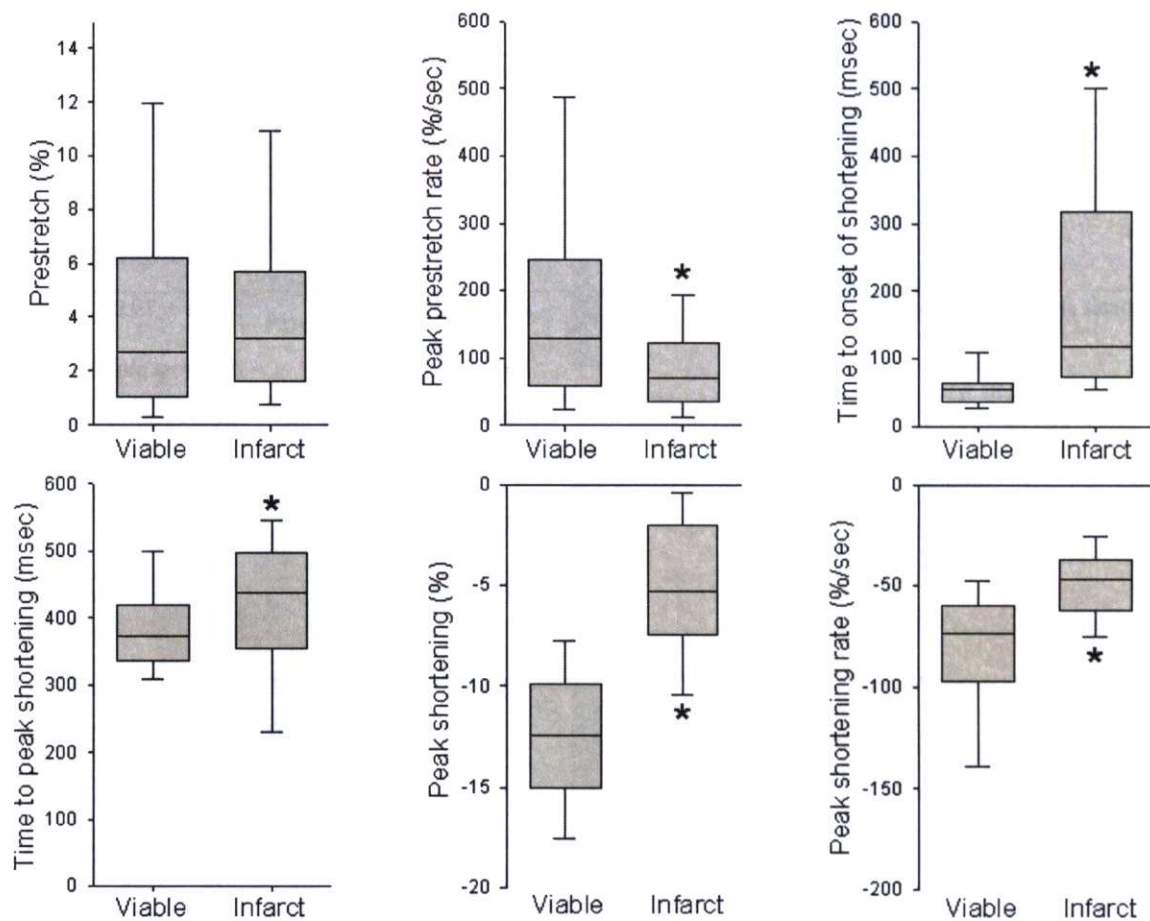


Figure 9-9: Comparison of mechanical indices between viable vs. infarct myocardium. These plots contain the pooled data from all the data points from all animals. The boundary of the box closest to zero indicates the 25th percentile, a line within the box marks the median, and the boundary of the box farthest from zero indicates the 75th percentile. Whiskers above and below the box indicate the 90th and 10th percentiles. *: P<0.05 vs. viable myocardium.

9.4.4 Correlation between prestretch and electromechanical indices

There was a significant correlation between prestretch and peak shortening rate in the viable myocardium (Figure 9-10).

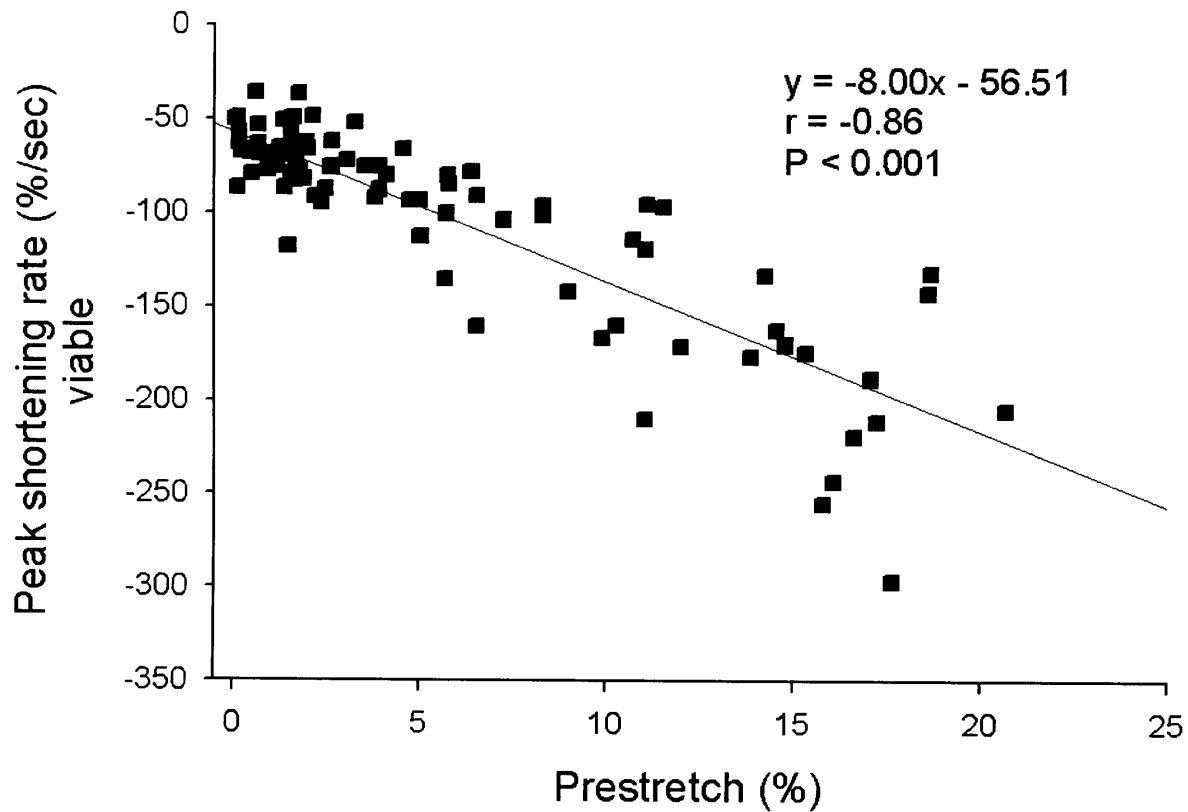


Figure 9-10: Correlation between prestretch and peak shortening rate in the viable myocardium in one animal ($r=-0.75$, $P<0.001$).

The correlation between prestretch and no other mechanical indices were consistently significant (Figure 9-11). The correlation between prestretch and ARI was analyzed in the prestretch region, which was the viable myocardium mostly in the lateral LV. The spatial distribution of greater prestretch was very similar to the distribution of longer ARI (Figure 9-12). A total of 24 ± 6 data points out of 144 in each heart were used for analysis. Figure 9-13 shows a strong correlation between prestretch and ARI in one animal ($r=0.89$, $P<0.001$). This correlation was consistently significant among all animals (Figure 9-11).

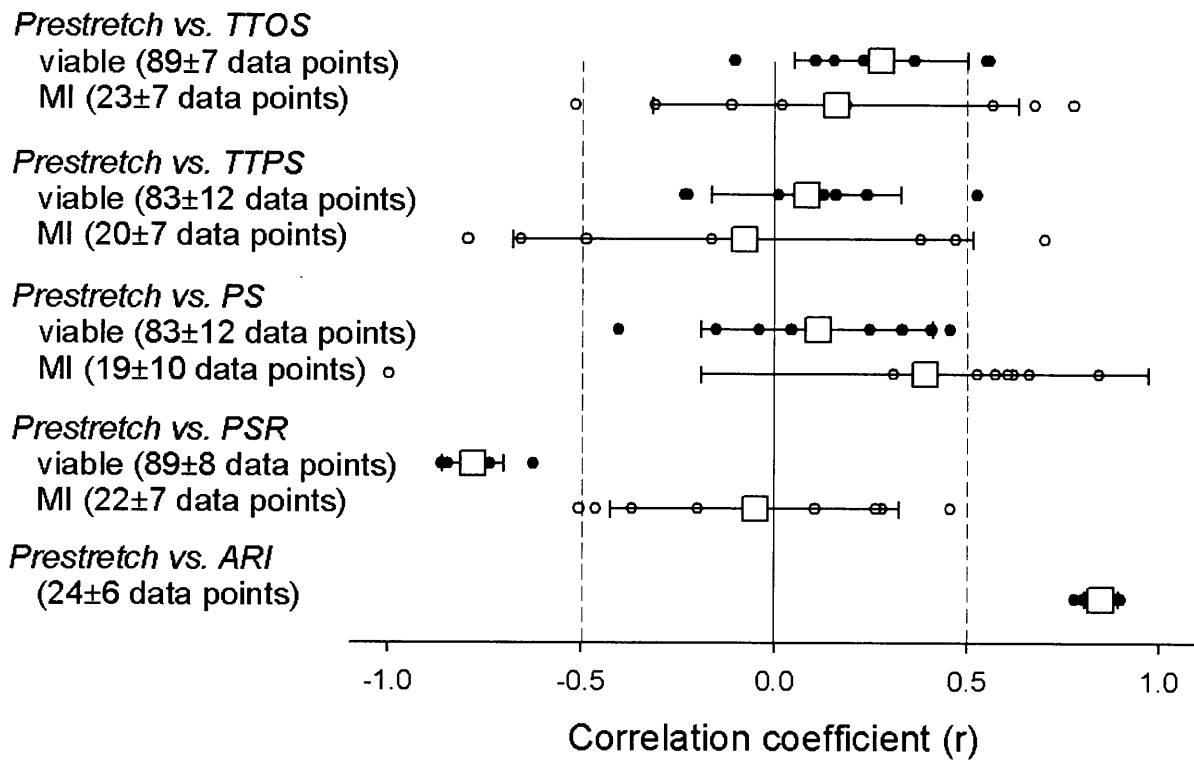


Figure 9-11: *Correlation coefficients for each animal.* Individual correlation coefficients are shown in closed (viable myocardium) and open (infarct myocardium) circles, and the open squares indicate mean \pm SD of the correlation coefficient in each animal. The number of data points per animal (mean \pm SD) to calculate each correlation coefficient is also shown. The horizontal dashed lines indicate $|r|=0.5$. TTOS, time to onset of shortening; TTPS, time to peak shortening; PS, peak shortening; PSR, peak shortening rate; ARI, activation recovery interval.

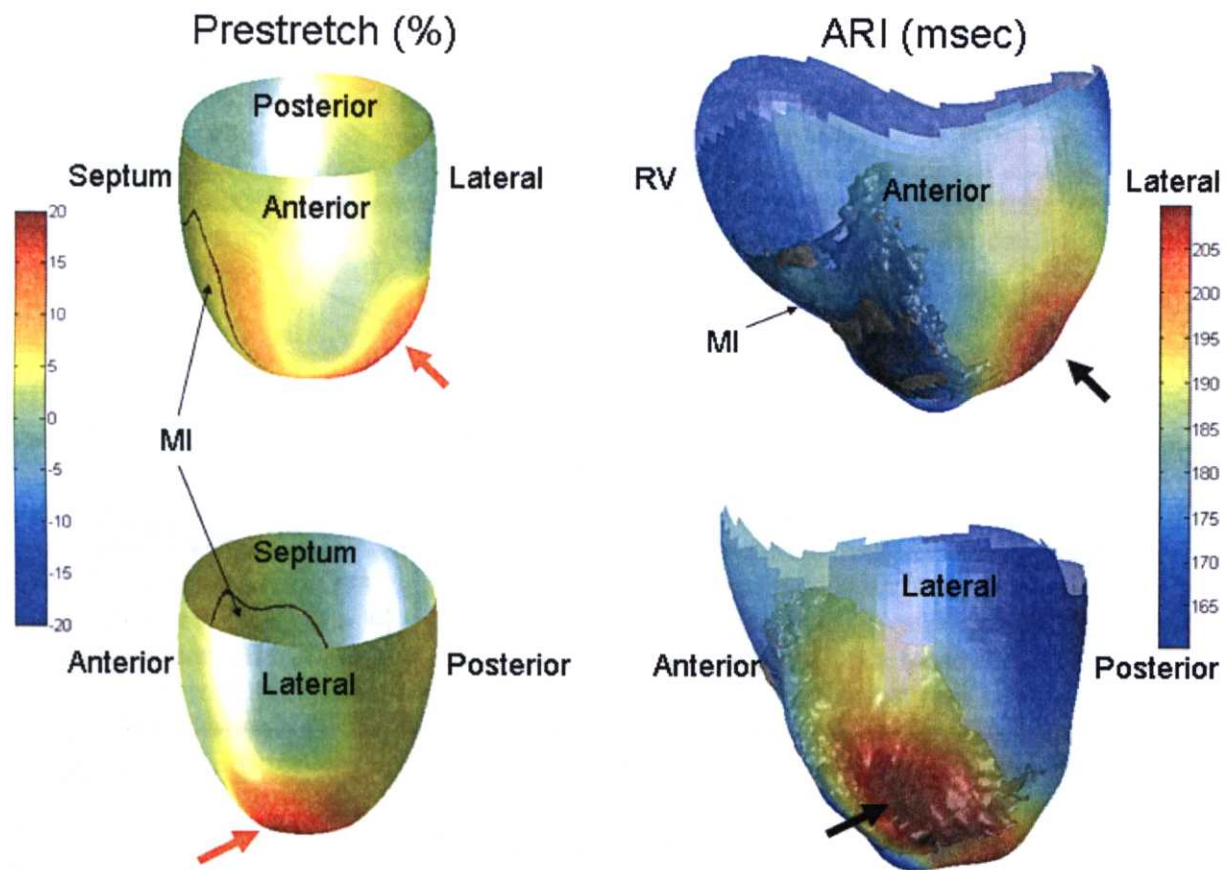


Figure 9-12: *Spatial distribution of prestretch and ARI in one animal.* The prolate ellipsoid mesh on the left represents prestretch (color-coded in %) derived from the cine-DENSE images, whereas the epicardial mesh on the right represents ARI (color-coded in msec) derived from the electrical sock measurement. The spatial distribution of greater prestretch (red arrow) was very similar to the distribution of longer ARI (black arrow).

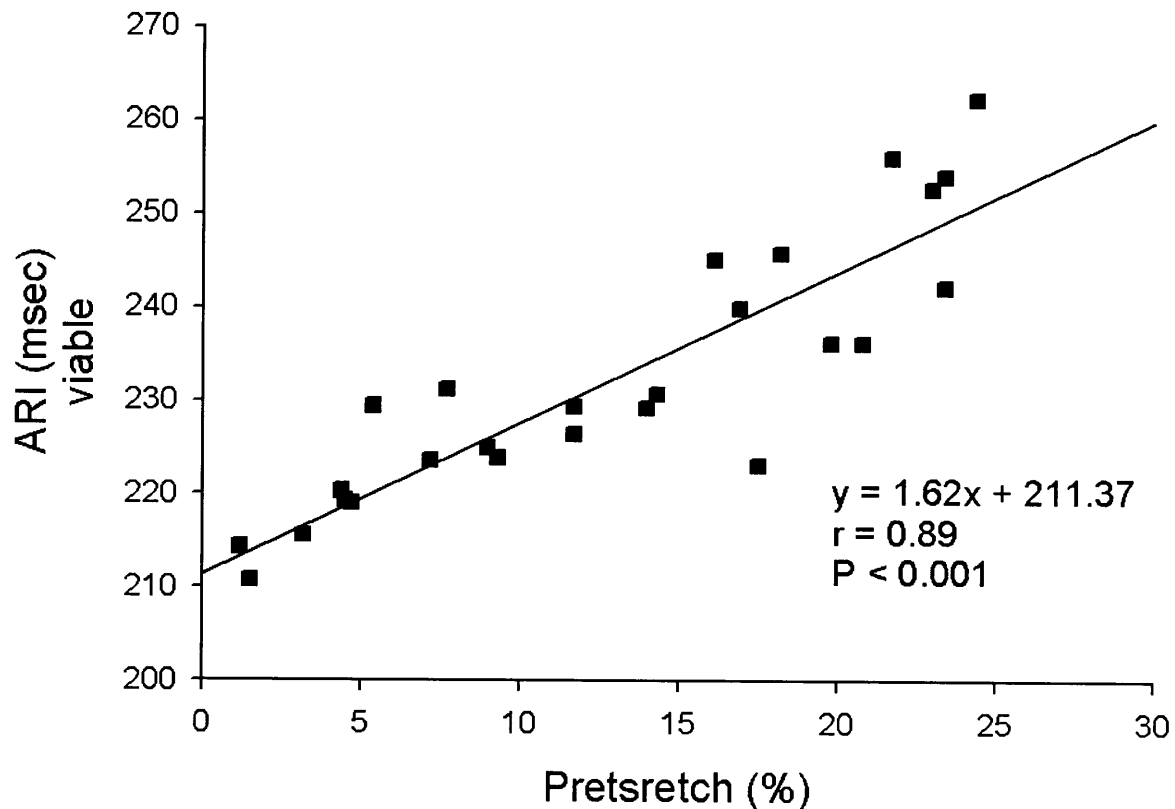


Figure 9-13: Correlation between prestretch and ARI in the prestretch region in one animal ($r=0.92$, $P<0.001$).

9.5 Discussion

9.5.1 Overview

The present study combined noninvasive MR-based techniques and invasive electrical measurements to examine the anatomical correlation of abnormal myocardial stretch and ARI in chronic MI. The quantitative mechanics using the cine-DENSE MRI demonstrates excellent agreement with that of tagged MRI (137), and cine-DENSE MRI requires less user input for post-processing than tagged MRI (252). Furthermore, high temporal resolution (9ms) allowed characterization of the timing, location, and magnitude of prestretch with high fidelity.

Although alteration of APD in response to acute loading has been studied at the global ventricular level, this is the first study to quantitatively demonstrate the magnitude-dependent mechano-electrical feedback (MEF) at a local level *in vivo*. The regionally heterogeneous prestretch likely generates a heterogeneous distribution APD, which results in an increased dispersion of repolarization and thus increased susceptibility to ventricular tachyarrhythmia. This finding is consistent with a recent report that the presence of left bundle branch block and resultant mechanical dyssynchrony in patients with heart failure is an independent risk factor of all cause mortality and sudden death (28)

9.5.2 Animal model of chronic myocardial infarction with substrate for sudden cardiac death

The occlusion-reperfusion MI model in the present study reflects a clinical scenario where acute coronary artery occlusion is followed by revascularization procedures, which is clinically associated with inducible VT (136). A closed-chest animal model of chronic MI within the first month after MI was used, because the risk of SCD is highest in this time period (220). Sustained monomorphic VT was inducible in all the animals studied, which confirms that those hearts have a substrate for SCD.

9.5.3 Mechanical characteristics of prestretch in chronic myocardial infarction

Prestretch appeared in early systole when the majority of the LV myocardium has not started contraction yet (Figure 9-8). This suggests that prestretch is not initiated by contraction of other ventricular regions, but by ventricular filling, likely due to atrial contraction. Diastolic expansion of the MI tissue is limited due to its 'stiff' material property relative to that of the viable myocardium, thus the region of largest expansion coincides with the more elastic, viable myocardium opposite to the MI. As a result, the regional pattern of prestretch was similar to that of normal human heart, being lowest in the septum and highest in the posterolateral region (82, 272). The posterolateral region opposite to the MI experiences largest and quickest prestretch, and quickest shortening (Figure 9-8A, B, F). Prestretch significantly correlated with peak shortening rate (Figure 9-10) which may reflect the regional Frank-Starling mechanism (272). However, no significant correlation was observed between prestretch and other mechanical indices (Figure 9-11). This implies disruption of the regional Frank-Starling mechanism in chronic MI, due to significantly depressed mechanical function in the infarct myocardium (Figure 9-9).

9.5.4 Prestretch and stretch-induced arrhythmia

The magnitude of prestretch in the data was substantially higher than those reported in normal human heart (10% vs. 4-6%) (82, 272) (Table 9-3). Because the magnitude of stretch is important in the induction of stretch-induced arrhythmia (55, 91, 128, 139, 263), these results support the involvement of prestretch in triggering fatal arrhythmia in chronic MI. In addition, the relatively long time period of prestretch (Figure 9-7) sufficiently covers the vulnerable window for stretch-induced arrhythmia (142), thus provide a mechanistic support for SCD in this population.

The results suggest that prestretch in chronic MI prolongs local ARI in a magnitude-dependent manner (Figure 9-10, 9-11, 9-12). This finding is consistent with a recent report by Nishimura *et al* using a carbon fiber technique and voltage-sensitive dye in single ventricular myocytes in rat (190). In contrast, earlier studies show that acute loading can shorten (204, 262) or prolong (170, 227) APD, possibly mediated by SACs (118), beta-adrenergic receptor activation (153) or actin cytoskeleton (190). One possible factor to explain the finding in light of these studies is the timing of stretch. Stretch results in shortening of APD during the early plateau phase and prolongation of APD at later stages of repolarization (90, 141, 146, 261). The results show that prestretch persists until 240-260msec, and the relatively long period of prestretch may cause consistent prolongation of APD in the region of prestretch. Another possible factor is that structurally remodeled hearts with chronic MI *in vivo* was used. Stretch-induced MEF was mostly studied in isolated normal rabbit heart (26, 80, 153, 204, 227, 262), and electrophysiological properties, including conduction velocity and MEF, of the structurally

remodeled myocardium are most likely different from those of the normal myocardium. For example, the myofiber and laminar structure of the myocardium are the structural bases of the orthogonal anisotropy of electrical propagation (116, 150), and these cardiac microstructures undergo significant alterations in the structurally remodeled hearts in a regionally heterogeneous manner (20, 110).

9.5.5 Clinical implications

The findings have two important clinical implications. First, the MR-guided, noninvasive quantification of prestretch may help identify the population at risk for SCD, along with other promising noninvasive diagnostic techniques including signal-averaged ECG (62), T-wave alternans (TWA) (36) and heart rate variability (HRV) (49). Further studies are needed to assess the risk of SCD in human patients with prestretch.

Second, the MR-guided quantification of prestretch may guide early interventions as primary prevention of SCD. Early interventions to modulate prestretch by multisite pacing combined with pharmacological interventions to suppress stretch-activated arrhythmia may be beneficial in reducing SCD. In addition, as demonstrated in CRT trials, suppression of prestretch would also prevent and even reverse structural remodeling in the viable myocardium, which would further reduce mortality in the longer period (99).

9.5.6 Limitations

Control studies were not conducted, therefore the electromechanical indices were not compared between control and infarct animals. The heart rate during electrical measurements was significantly higher than that of mechanical measurements (129 ± 13 vs. 97 ± 28 bpm, $P=0.019$), most likely due to reduced preload associated with thoracotomy. Earlier studies suggest that ARI measurements are sensitive to loading conditions, thus the magnitudes of ARI may have been underestimated. The LV mechanics was examined in anesthetized, closed-chest swine. Therefore, the results may not precisely reflect the cardiac mechanics in conscious animals. Species difference (swine vs. human) is another factor to consider when these results are clinically extrapolated. The strain data in the present study describe the average transmural mechanics in the LV myocardium *in vivo*. Although significant transmural variations in timing and magnitude of prestretch have been described (16), the aim of the present study was to identify regional variations, not transmural variations, of cardiac strains. To maintain a sufficient signal-to-noise ratio (SNR), the tissue-tracking MRI sequence required an interval for T_1 recovery between the last phase in one cardiac cycle and the beginning of the next cardiac cycle. Therefore the mechanical indices for an entire cardiac cycle was not studied. However, the aim of the present study was to examine systolic shortening, and the 85% coverage of the cardiac cycle (Table 9-2) was more than sufficient for this objective.

9.6 Conclusions

Prestretch in chronic MI prolongs local ARI in a magnitude-dependent manner in swine with a substrate for SCD. The stretch-induced ARI prolongation may increase the dispersion of repolarization and thus susceptibility to ventricular tachyarrhythmia. Early interventions to reduce prestretch may help reduce SCD in patients with chronic MI.

Chapter 10

Thesis conclusions

The overall goal of the thesis was to assess anatomical correlation between cardiac mechanics and electrophysiology *in vivo*, and to investigate whether it is possible to predict electrical behaviors from mechanical behaviors of the heart. There were six specific aims to achieve this goal, and the conclusions from these aims are:

Aim 1: LV mechanics during early relaxation involves substantial deformation of fiber and sheet structures with significant transmural heterogeneity. Predominant epicardial stretch along myofibers during isovolumic relaxation appears to drive global torsional recoil to aid early diastolic filling (Chapter 4)

Aim 2: Enhanced filling in volume-overload hypertrophy is achieved by enhanced sheet shear early in diastole. These results provide the first evidence that changes in motion of radially oriented laminar sheets may play an important functional role in pathology of diastolic dysfunction in this model (Chapter 5).

Aim 3: Despite lack of evidence of significant transmural gradient in electrical repolarization *in vivo*, there is transmural dispersion of myofiber relaxation as well as shortening (Chapter 6).

Aim 4: Normal sheet extension and wall thickening immediately after activation may require normal transmural activation sequence, whereas sheet shear deformation may be determined by local anatomy. (Chapter 7).

Aim 5: The infarct border zone is characterized by abnormal mechanics directly coupled with normal electrical depolarization. This indicates that impaired function in the border zone is not contributed by electrical factors but results from mechanical interaction between ischemic and normal myocardium (Chapter 8)

Aim 6: Prestretch in chronic MI prolongs local ARI in a magnitude-dependent manner in swine with a substrate for SCD. The stretch-induced ARI prolongation may increase the dispersion of repolarization and thus susceptibility to ventricular tachyarrhythmia. Early interventions to reduce prestretch may help reduce SCD in patients with chronic MI (Chapter 9).

These results underscore the fact that cardiac anatomy (e.g. fiber, sheet structures), electrophysiology (e.g. activation sequence) and mechanics (e.g. shear, prestretch) are indispensably intertwined, thus interdependent. Although this thesis focused on prediction of the susceptibility to SCD as a clinical output, the interdependence of anatomy, electrophysiology and mechanics could be further utilized in future research to extract clinically relevant information.

Bibliography

References

1. European Study Group on Diastolic Heart Failure. How to diagnose diastolic heart failure. *Eur Heart J* 19: 990-1003, 1998.
2. Position of the American Heart Association on the use of research animals. A statement for health professionals from a task force appointed by the Board of Directors of the American Heart Association. *Circ Res* 57: 330-331, 1985.
3. Aletras AH, Balaban RS, and Wen H. High-resolution strain analysis of the human heart with fast-DENSE. *J Magn Reson* 140: 41-57, 1999.
4. Aletras AH, Ding S, Balaban RS, and Wen H. DENSE: displacement encoding with stimulated echoes in cardiac functional MRI. *J Magn Reson* 137: 247-252, 1999.
5. Aletras AH and Wen H. Mixed echo train acquisition displacement encoding with stimulated echoes: an optimized DENSE method for in vivo functional imaging of the human heart. *Magn Reson Med* 46: 523-534, 2001.
6. Alexander RS. Viscoelastic determinants of muscle contractility and "cardiac tone." *Fed Proc* 21: 1001, 1962.
7. Antzelevitch C. Cardiac repolarization. The long and short of it. *Europace* 7 Suppl 2: 3-9, 2005.
8. Antzelevitch C and Fish J. Electrical heterogeneity within the ventricular wall. *Basic Res Cardiol* 96: 517-527, 2001.
9. Antzelevitch C, Shimizu W, Yan GX, Sicouri S, Weissenburger J, Nesterenko VV, Burashnikov A, Di Diego J, Saffitz J, and Thomas GP. The M cell: its contribution to the ECG and to normal and abnormal electrical function of the heart. *J Cardiovasc Electrophysiol* 10: 1124-1152, 1999.
10. Anyukhovsky EP, Sosunov EA, Gainullin RZ, and Rosen MR. The controversial M cell. *J Cardiovasc Electrophysiol* 10: 244-260, 1999.
11. Anyukhovsky EP, Sosunov EA, and Rosen MR. Regional differences in electrophysiological properties of epicardium, midmyocardium, and endocardium. In vitro and in vivo correlations. *Circulation* 94: 1981-1988, 1996.
12. Arts T, Costa KD, Covell JW, and McCulloch AD. Relating myocardial laminar architecture to shear strain and muscle fiber orientation. *Am J Physiol Heart Circ Physiol* 280: H2222-2229, 2001.
13. Arts T, Prinzen FW, Snoeckx LH, Rijcken JM, and Reneman RS. Adaptation of cardiac structure by mechanical feedback in the environment of the cell: a model study. *Biophys J* 66: 953-961, 1994.
14. Arts T and Reneman RS. Dynamics of left ventricular wall and mitral valve mechanics--a model study. *J Biomech* 22: 261-271, 1989.
15. Arts T, Reneman RS, and Veenstra PC. A model of the mechanics of the left ventricle. *Ann Biomed Eng* 7: 299-318, 1979.
16. Ashikaga H, Coppola BA, Hopenfeld B, Leifer ES, McVeigh ER, and Omens JH. Transmural dispersion of myofiber mechanics: implications for electrical heterogeneity in vivo. *J Am Coll Cardiol* In Press, 2006.
17. Ashikaga H, Criscione JC, Omens JH, Covell JW, and Ingels NB, Jr. Transmural left ventricular mechanics underlying torsional recoil during relaxation. *Am J Physiol Heart Circ Physiol* 286: H640-647, 2004.
18. Ashikaga H, Hopenfeld B, and McVeigh E. MR-guided evaluation of post-infarction ventricular tachycardia. *International Society for Magnetic Resonance in Medicine, 14th Scientific Meeting and Exhibition* Seattle, WA: May 6-12, 2006 (abstract), 2006.
19. Ashikaga H, Mickelsen SR, Ennis DB, Rodriguez I, Kellman P, Wen H, and McVeigh ER. Electromechanical analysis of infarct border zone in chronic myocardial infarction. *Am J Physiol Heart Circ Physiol*, 2005.
20. Ashikaga H, Omens JH, and Covell JW. Time-dependent remodeling of transmural architecture underlying abnormal ventricular geometry in chronic volume overload heart failure. *Am J Physiol Heart Circ Physiol* 287: H1994-2002, 2004.
21. Ashikaga H, Omens JH, Ingels NB, Jr., and Covell JW. Transmural mechanics at left ventricular epicardial pacing site. *Am J Physiol Heart Circ Physiol* 286: H2401-H2407, 2004.
22. Ashikaga H, Omens JH, Ingels NB, Jr., and Covell JW. Transmural mechanics at left ventricular epicardial pacing site. *Am J Physiol Heart Circ Physiol* 286: H2401-2407, 2004.
23. Auricchio A, Stellbrink C, Block M, Sack S, Vogt J, Bakker P, Klein H, Kramer A, Ding J, Salo R, Tockman B, Pochet T, and Spinelli J. Effect of pacing chamber and atrioventricular delay on acute systolic

- function of paced patients with congestive heart failure. The Pacing Therapies for Congestive Heart Failure Study Group. The Guidant Congestive Heart Failure Research Group. *Circulation* 99: 2993-3001, 1999.
24. **Axel L.** Biomechanical dynamics of the heart with MRI. *Annu Rev Biomed Eng* 4: 321-347, 2002.
 25. **Axel L and Dougherty L.** MR imaging of motion with spatial modulation of magnetization. *Radiology* 171: 841-845, 1989.
 26. **Babuty D and Lab M.** Heterogeneous changes of monophasic action potential induced by sustained stretch in atrium. *J Cardiovasc Electrophysiol* 12: 323-329, 2001.
 27. **Babuty D and Lab MJ.** Mechanoelectric contributions to sudden cardiac death. *Cardiovasc Res* 50: 270-279, 2001.
 28. **Baldasseroni S, Opasich C, Gorini M, Lucci D, Marchionni N, Marini M, Campana C, Perini G, Deorsola A, Masotti G, Tavazzi L, and Maggioni AP.** Left bundle-branch block is associated with increased 1-year sudden and total mortality rate in 5517 outpatients with congestive heart failure: a report from the Italian network on congestive heart failure. *Am Heart J* 143: 398-405, 2002.
 29. **Barr RC and Spach MS.** Sampling rates required for digital recording of intracellular and extracellular cardiac potentials. *Circulation* 55: 40-48, 1977.
 30. **Bayes de Luna A, Coumel P, and Leclercq JF.** Ambulatory sudden cardiac death: mechanisms of production of fatal arrhythmia on the basis of data from 157 cases. *Am Heart J* 117: 151-159, 1989.
 31. **Bazett JC.** An analysis of time relation of electrocardiograms. *Heart* 7: 353-367, 1920.
 32. **Bell SP, Nyland L, Tischler MD, McNabb M, Granzier H, and LeWinter MM.** Alterations in the determinants of diastolic suction during pacing tachycardia. *Circ Res* 87: 235-240, 2000.
 33. **Beyar R and Sideman S.** The dynamic twisting of the left ventricle: a computer study. *Ann Biomed Eng* 14: 547-562, 1986.
 34. **Beyar R, Yin FC, Hausknecht M, Weisfeldt ML, and Kass DA.** Dependence of left ventricular twist-radial shortening relations on cardiac cycle phase. *Am J Physiol* 257: H1119-1126, 1989.
 35. **Blanc JJ, Etienne Y, Gilard M, Mansourati J, Munier S, Bosch J, Benditt DG, and Lurie KG.** Evaluation of different ventricular pacing sites in patients with severe heart failure: results of an acute hemodynamic study. *Circulation* 96: 3273-3277, 1997.
 36. **Bloomfield DM, Bigger JT, Steinman RC, Namerow PB, Parides MK, Curtis AB, Kaufman ES, Davidenko JM, Shinn TS, and Fontaine JM.** Microvolt T-wave alternans and the risk of death or sustained ventricular arrhythmias in patients with left ventricular dysfunction. *J Am Coll Cardiol* 47: 456-463, 2006.
 37. **Bogaert J and Rademakers FE.** Regional nonuniformity of normal adult human left ventricle. *Am J Physiol Heart Circ Physiol* 280: H610-620, 2001.
 38. **Bovendeerd PH, Arts T, Huyghe JM, van Campen DH, and Reneman RS.** Dependence of local left ventricular wall mechanics on myocardial fiber orientation: a model study. *J Biomech* 25: 1129-1140, 1992.
 39. **Braunwald E.** Shattuck lecture--cardiovascular medicine at the turn of the millennium: triumphs, concerns, and opportunities. *N Engl J Med* 337: 1360-1369, 1997.
 40. **Bristow MR, Saxon LA, Boehmer J, Krueger S, Kass DA, De Marco T, Carson P, DiCarlo L, DeMets D, White BG, DeVries DW, and Feldman AM.** Cardiac-resynchronization therapy with or without an implantable defibrillator in advanced chronic heart failure. *N Engl J Med* 350: 2140-2150, 2004.
 41. **Buchalter MB, Rademakers FE, Weiss JL, Rogers WJ, Weisfeldt ML, and Shapiro EP.** Rotational deformation of the canine left ventricle measured by magnetic resonance tagging: effects of catecholamines, ischaemia, and pacing. *Cardiovasc Res* 28: 629-635, 1994.
 42. **Buchalter MB, Weiss JL, Rogers WJ, Zerhouni EA, Weisfeldt ML, Beyar R, and Shapiro EP.** Noninvasive quantification of left ventricular rotational deformation in normal humans using magnetic resonance imaging myocardial tagging. *Circulation* 81: 1236-1244, 1990.
 43. **Buckberg GD, Castella M, Gharib M, and Saleh S.** Active myocyte shortening during the 'isovolumetric relaxation' phase of diastole is responsible for ventricular suction; 'systolic ventricular filling'. *Eur J Cardiothorac Surg* 29 Suppl 1: S98-106, 2006.
 44. **Buckberg GD, Weisfeldt ML, Ballester M, Beyar R, Burkhoff D, Coghlan HC, Doyle M, Epstein ND, Gharib M, Ideker RE, Ingels NB, LeWinter MM, McCulloch AD, Pohost GM, Reinlib LJ, Sahn DJ, Sopko G, Spinale FG, Spotnitz HM, Torrent-Guasp F, and Shapiro EP.** Left ventricular form and function: scientific priorities and strategic planning for development of new views of disease. *Circulation* 110: e333-336, 2004.
 45. **Burgess MJ, Green LS, Millar K, Wyatt R, and Abildskov JA.** The sequence of normal ventricular recovery. *Am Heart J* 84: 660-669, 1972.
 46. **Burkhoff D, Maurer MS, and Packer M.** Heart failure with a normal ejection fraction: is it really a disorder of diastolic function? *Circulation* 107: 656-658, 2003.
 47. **Buxton AE, Lee KL, DiCarlo L, Gold MR, Greer GS, Prystowsky EN, O'Toole MF, Tang A, Fisher JD, Coromilas J, Talajic M, and Hafley G.** Electrophysiologic testing to identify patients with coronary artery

disease who are at risk for sudden death. Multicenter Unsustained Tachycardia Trial Investigators. *N Engl J Med* 342: 1937-1945, 2000.

48. Buxton AE, Lee KL, Hafley GE, Wyse DG, Fisher JD, Lehmann MH, Pires LA, Gold MR, Packer DL, Josephson ME, Prystowsky EN, and Talajic MR. Relation of ejection fraction and inducible ventricular tachycardia to mode of death in patients with coronary artery disease: an analysis of patients enrolled in the multicenter unsustained tachycardia trial. *Circulation* 106: 2466-2472, 2002.

49. Camm AJ, Pratt CM, Schwartz PJ, Al-Khalidi HR, Spyt MJ, Holroyde MJ, Karam R, Sonnenblick EH, and Brum JM. Mortality in patients after a recent myocardial infarction: a randomized, placebo-controlled trial of azimilide using heart rate variability for risk stratification. *Circulation* 109: 990-996, 2004.

50. Caprihan A, Griffey RH, and Fukushima E. Velocity imaging of slow coherent flows using stimulated echoes. *Magn Reson Med* 15: 327-333, 1990.

51. Carabello BA. Aortic regurgitation: Hemodynamic determinants of prognosis. In: *Aortic Regurgitation: Medical and Surgical Management*, edited by DiSesa VJ. New York: Marcel Dekker, Inc, 1986.

52. Cazeau S, Ritter P, Lazarus A, Gras D, Backdach H, Mundler O, and Mugica J. Multisite pacing for end-stage heart failure: early experience. *Pacing Clin Electrophysiol* 19: 1748-1757, 1996.

53. Cazorla O, Freiburg A, Helmes M, Centner T, McNabb M, Wu Y, Trombitas K, Labeit S, and Granzier H. Differential expression of cardiac titin isoforms and modulation of cellular stiffness. *Circ Res* 86: 59-67, 2000.

54. Chauhan VS, Downar E, Nanthakumar K, Parker JD, Ross HJ, Chan W, and Picton P. Increased ventricular repolarization heterogeneity in patients with ventricular arrhythmia vulnerability and cardiomyopathy: a human in vivo study. *Am J Physiol Heart Circ Physiol* 290: H79-86, 2006.

55. Chen RL, Penny DJ, Greve G, and Lab MJ. Stretch-induced regional mechanoelectric dispersion and arrhythmia in the right ventricle of anesthetized lambs. *Am J Physiol Heart Circ Physiol* 286: H1008-1014, 2004.

56. Cheng A, Langer F, Nguyen TC, Malinowski M, Ennis DB, Daughters GT, Ingels NB, Jr., and Miller DC. Transmural left ventricular shear strain alterations adjacent to and remote from infarcted myocardium. *J Heart Valve Dis* 15: 209-218; discussion 218, 2006.

57. Cheng A, Langer F, Rodriguez F, Criscione JC, Daughters GT, Miller DC, and Ingels NB, Jr. Transmural cardiac strains in the lateral wall of the ovine left ventricle. *Am J Physiol Heart Circ Physiol* 288: H1546-1556, 2005.

58. Cleland JG, Daubert JC, Erdmann E, Freemantle N, Gras D, Kappenberger L, and Tavazzi L. The effect of cardiac resynchronization on morbidity and mortality in heart failure. *N Engl J Med* 352: 1539-1549, 2005.

59. Cleophas TJ and Zwinderman AH. Beta-blockers and heart failure: meta-analysis of mortality trials. *Int J Clin Pharmacol Ther* 39: 383-388, 2001.

60. Cobb LA, Fahrenbruch CE, Olsufka M, and Copass MK. Changing incidence of out-of-hospital ventricular fibrillation, 1980-2000. *Jama* 288: 3008-3013, 2002.

61. Cohn JN. Post-MI remodeling. *Clin Cardiol* 16: II21-24, 1993.

62. Cook JR, Flack JE, Gregory CA, Deaton DW, Rousou JA, and Engelman RM. Influence of the preoperative signal-averaged electrocardiogram on left ventricular function after coronary artery bypass graft surgery in patients with left ventricular dysfunction. The CABG Patch Trial. *Am J Cardiol* 82: 285-289, 1998.

63. Cordeiro JM, Greene L, Heilmann C, Antzelevitch D, and Antzelevitch C. Transmural heterogeneity of calcium activity and mechanical function in the canine left ventricle. *Am J Physiol Heart Circ Physiol* 286: H1471-1479, 2004.

64. Corin WJ, Murakami T, Monrad ES, Hess OM, and Krayenbuehl HP. Left ventricular passive diastolic properties in chronic mitral regurgitation. *Circulation* 83: 797-807, 1991.

65. Costa KD, May-Newman K, Farr D, O'Dell WG, McCulloch AD, and Omens JH. Three-dimensional residual strain in midanterior canine left ventricle. *Am J Physiol* 273: H1968-1976, 1997.

66. Costa KD, Takayama Y, McCulloch AD, and Covell JW. Laminar fiber architecture and three-dimensional systolic mechanics in canine ventricular myocardium. *Am J Physiol* 276: H595-607, 1999.

67. Covell JW. Factors influencing diastolic function. Possible role of the extracellular matrix. *Circulation* 81: III155-158, 1990.

68. Criscione JC, Rodriguez F, and Miller DC. The myocardial band: simplicity can be a weakness. *Eur J Cardiothorac Surg* 28: 363-364; author reply 364-367, 2005.

69. Daniel TM, Boineau JP, and Sabiston DC, Jr. Comparison of human ventricular activation with a canine model in chronic myocardial infarction. *Circulation* 44: 74-89, 1971.

70. Daubert JP, Zareba W, Hall WJ, Schuger C, Corsello A, Leon AR, Andrews ML, McNitt S, Huang DT, and Moss AJ. Predictive value of ventricular arrhythmia inducibility for subsequent ventricular tachycardia or ventricular fibrillation in Multicenter Automatic Defibrillator Implantation Trial (MADIT) II patients. *J Am Coll Cardiol* 47: 98-107, 2006.

71. **Dauterman KW, Massie BM, and Gheorghiade M.** Heart failure associated with preserved systolic function: a common and costly clinical entity. *Am Heart J* 135: S310-319, 1998.
72. **Davis HT, DeCamilla J, Bayer LW, and Moss AJ.** Survivorship patterns in the posthospital phase of myocardial infarction. *Circulation* 60: 1252-1258, 1979.
73. **Davis JS, Hassanzadeh S, Winitsky S, Lin H, Satorius C, Vemuri R, Aletras AH, Wen H, and Epstein ND.** The overall pattern of cardiac contraction depends on a spatial gradient of myosin regulatory light chain phosphorylation. *Cell* 107: 631-641, 2001.
74. **de Vreede-Swagemakers JJ, Gorgels AP, Dubois-Arbouw WI, van Ree JW, Daemen MJ, Houben LG, and Wellens HJ.** Out-of-hospital cardiac arrest in the 1990's: a population-based study in the Maastricht area on incidence, characteristics and survival. *J Am Coll Cardiol* 30: 1500-1505, 1997.
75. **Delhaas T, Arts T, Prinzen FW, and Reneman RS.** Relation between regional electrical activation time and subepicardial fiber strain in the canine left ventricle. *Pflugers Arch* 423: 78-87, 1993.
76. **Di Diego JM, Belardinelli L, and Antzelevitch C.** Cisapride-induced transmural dispersion of repolarization and torsade de pointes in the canine left ventricular wedge preparation during epicardial stimulation. *Circulation* 108: 1027-1033, 2003.
77. **Dou J, Tseng WY, Reese TG, and Wedeen VJ.** Combined diffusion and strain MRI reveals structure and function of human myocardial laminar sheets in vivo. *Magn Reson Med* 50: 107-113, 2003.
78. **Duff HJ, Martin JM, and Rahmberg M.** Time-dependent change in electrophysiologic milieu after myocardial infarction in conscious dogs. *Circulation* 77: 209-220, 1988.
79. **Durrer D, van Dam RT, Freud GE, Janse MJ, Meijler FL, and Arzbacher RC.** Total excitation of the isolated human heart. *Circulation* 41: 899-912, 1970.
80. **Eckardt L, Kirchhof P, Monnig G, Breithardt G, Borggrefe M, and Haverkamp W.** Modification of stretch-induced shortening of repolarization by streptomycin in the isolated rabbit heart. *J Cardiovasc Pharmacol* 36: 711-721, 2000.
81. **el-Sherif N, Caref EB, Yin H, and Restivo M.** The electrophysiological mechanism of ventricular arrhythmias in the long QT syndrome. Tridimensional mapping of activation and recovery patterns. *Circ Res* 79: 474-492, 1996.
82. **Ennis DB, Epstein FH, Kellman P, Fananapazir L, McVeigh ER, and Arai AE.** Assessment of regional systolic and diastolic dysfunction in familial hypertrophic cardiomyopathy using MR tagging. *Magn Reson Med* 50: 638-642, 2003.
83. **Epstein FH, Wolff SD, and Arai AE.** Segmented k-space fast cardiac imaging using an echo-train readout. *Magn Reson Med* 41: 609-613, 1999.
84. **Epstein FH, Yang Z, Gilson WD, Berr SS, Kramer CM, and French BA.** MR tagging early after myocardial infarction in mice demonstrates contractile dysfunction in adjacent and remote regions. *Magn Reson Med* 48: 399-403, 2002.
85. **Escobedo LG and Zack MM.** Comparison of sudden and nonsudden coronary deaths in the United States. *Circulation* 93: 2033-2036, 1996.
86. **Fann JJ, Sarris GE, Ingels NB, Jr., Niczyporuk MA, Yun KL, Daughters GT, 2nd, Derby GC, and Miller DC.** Regional epicardial and endocardial two-dimensional finite deformations in canine left ventricle. *Am J Physiol* 261: H1402-1410, 1991.
87. **Faris OP, Evans FJ, Dick AJ, Raman VK, Ennis DB, Kass DA, and McVeigh ER.** Endocardial versus epicardial electrical synchrony during LV free-wall pacing. *Am J Physiol Heart Circ Physiol* 285: H1864-1870, 2003.
88. **Faris OP, Evans FJ, Ennis DB, Helm PA, Taylor JL, Chesnick AS, Guttman MA, Ozturk C, and McVeigh ER.** Novel technique for cardiac electromechanical mapping with magnetic resonance imaging tagging and an epicardial electrode sock. *Ann Biomed Eng* 31: 430-440, 2003.
89. **Franz MR, Bargheer K, Rafflenbeul W, Haverich A, and Lichtlen PR.** Monophasic action potential mapping in human subjects with normal electrocardiograms: direct evidence for the genesis of the T wave. *Circulation* 75: 379-386, 1987.
90. **Franz MR, Burkhoff D, Yue DT, and Sagawa K.** Mechanically induced action potential changes and arrhythmia in isolated and in situ canine hearts. *Cardiovasc Res* 23: 213-223, 1989.
91. **Franz MR, Cima R, Wang D, Profitt D, and Kurz R.** Electrophysiological effects of myocardial stretch and mechanical determinants of stretch-activated arrhythmias. *Circulation* 86: 968-978, 1992.
92. **Frazier DW, Krassowska W, Chen PS, Wolf PD, Daniele ND, Smith WM, and Ideker RE.** Transmural activations and stimulus potentials in three-dimensional anisotropic canine myocardium. *Circ Res* 63: 135-146, 1988.
93. **Gallagher KP, Gerren RA, Choy M, Stirling MC, and Dysko RC.** Subendocardial segment length shortening at lateral margins of ischemic myocardium in dogs. *Am J Physiol* 253: H826-837, 1987.

94. **Gallagher KP, Gerren RA, Stirling MC, Choy M, Dysko RC, McManimon SP, and Dunham WR.** The distribution of functional impairment across the lateral border of acutely ischemic myocardium. *Circ Res* 58: 570-583, 1986.
95. **Gang ES, Bigger JT, Jr., and Livelli FD, Jr.** A model of chronic ischemic arrhythmias: the relation between electrically inducible ventricular tachycardia, ventricular fibrillation threshold and myocardial infarct size. *Am J Cardiol* 50: 469-477, 1982.
96. **Gang ES, Bigger JT, Jr., and Uhl EW.** Effects of timolol and propranolol on inducible sustained ventricular tachyarrhythmias in dogs with subacute myocardial infarction. *Am J Cardiol* 53: 275-281, 1984.
97. **Gardner PI, Ursell PC, Fenoglio JJ, Jr., and Wit AL.** Electrophysiologic and anatomic basis for fractionated electrograms recorded from healed myocardial infarcts. *Circulation* 72: 596-611, 1985.
98. **Garot J, Lima JA, Gerber BL, Sampath S, Wu KC, Bluemke DA, Prince JL, and Osman NF.** Spatially resolved imaging of myocardial function with strain-encoded MR: comparison with delayed contrast-enhanced MR imaging after myocardial infarction. *Radiology* 233: 596-602, 2004.
99. **Gasparini M, Auricchio A, Regoli F, Fantoni C, Kawabata M, Galimberti P, Pini D, Ceriotti C, Gronda E, Klersy C, Fratini S, and Klein HH.** Four-year efficacy of cardiac resynchronization therapy on exercise tolerance and disease progression: the importance of performing atrioventricular junction ablation in patients with atrial fibrillation. *J Am Coll Cardiol* 48: 734-743, 2006.
100. **Gerdes AM, Campbell SE, and Hilbelink DR.** Structural remodeling of cardiac myocytes in rats with arteriovenous fistulas. *Lab Invest* 59: 857-861, 1988.
101. **Gillum RF.** Geographic variation in sudden coronary death. *Am Heart J* 119: 380-389, 1990.
102. **Gillum RF.** Sudden coronary death in the United States: 1980-1985. *Circulation* 79: 756-765, 1989.
103. **Gilson WD, Yang Z, French BA, and Epstein FH.** Measurement of Myocardial Mechanics in Mice before and after Infarction using Multislice Displacement-Encoded MRI with 3D Motion Encoding. *Am J Physiol Heart Circ Physiol*, 2004.
104. **Goetz WA, Lansac E, Lim HS, Weber PA, and Duran CM.** Left ventricular endocardial longitudinal and transverse changes during isovolumic contraction and relaxation: a challenge. *Am J Physiol Heart Circ Physiol* 289: H196-201, 2005.
105. **Guccione JM, Costa KD, and McCulloch AD.** Finite element stress analysis of left ventricular mechanics in the beating dog heart. *J Biomech* 28: 1167-1177, 1995.
106. **Haake EM, Brown RW, Thompson MR, and Venkatesan R.** *Magnetic Resonance Imaging: Physical Principles and Sequence Design*. New Jersey: Wiley-Liss, 1999.
107. **Harrington KB, Rodriguez F, Cheng A, Langer F, Ashikaga H, Daughters GT, Criscione JC, Ingels NB, and Miller DC.** Direct measurement of transmural laminar architecture in the anterolateral wall of the ovine left ventricle: new implications for wall thickening mechanics. *Am J Physiol Heart Circ Physiol* 288: H1324-1330, 2005.
108. **Haws CW and Lux RL.** Correlation between in vivo transmembrane action potential durations and activation-recovery intervals from electrograms. Effects of interventions that alter repolarization time. *Circulation* 81: 281-288, 1990.
109. **Helm PA, Tseng HJ, Younes L, McVeigh ER, and Winslow RL.** Ex vivo 3D diffusion tensor imaging and quantification of cardiac laminar structure. *Magn Reson Med* 54: 850-859, 2005.
110. **Helm PA, Younes L, Beg MF, Ennis DB, Leclercq C, Faris OP, McVeigh E, Kass D, Miller MI, and Winslow RL.** Evidence of structural remodeling in the dyssynchronous failing heart. *Circ Res* 98: 125-132, 2006.
111. **Helmes M, Trombitas K, and Granzier H.** Titin develops restoring force in rat cardiac myocytes. *Circ Res* 79: 619-626, 1996.
112. **Herbots L, Maes F, D'Hooge J, Claus P, Dymarkowski S, Mertens P, Mortelmans L, Bijneens B, Bogaert J, Rademakers FE, and Sutherland GR.** Quantifying myocardial deformation throughout the cardiac cycle: a comparison of ultrasound strain rate, grey-scale M-mode and magnetic resonance imaging. *Ultrasound Med Biol* 30: 591-598, 2004.
113. **Herrmann KL, McCulloch AD, and Omens JH.** Glycated collagen cross-linking alters cardiac mechanics in volume-overload hypertrophy. *Am J Physiol Heart Circ Physiol* 284: H1277-1284, 2003.
114. **Holmes JW, Nunez JA, and Covell JW.** Functional implications of myocardial scar structure. *Am J Physiol* 272: H2123-2130, 1997.
115. **Holmes JW, Yamashita H, Waldman LK, and Covell JW.** Scar remodeling and transmural deformation after infarction in the pig. *Circulation* 90: 411-420, 1994.
116. **Hooks DA, Tomlinson KA, Marsden SG, LeGrice IJ, Smaill BH, Pullan AJ, and Hunter PJ.** Cardiac microstructure: implications for electrical propagation and defibrillation in the heart. *Circ Res* 91: 331-338, 2002.
117. **Hopenfeld B.** Spherical harmonic-based finite element meshing scheme for modelling current flow within the heart. *Med Biol Eng Comput* 42: 847-851, 2004.

118. **Hu H and Sachs F.** Stretch-activated ion channels in the heart. *J Mol Cell Cardiol* 29: 1511-1523, 1997.
119. **Huikuri HV, Castellanos A, and Myerburg RJ.** Sudden death due to cardiac arrhythmias. *N Engl J Med* 345: 1473-1482, 2001.
120. **Iimoto DS, Covell JW, and Harper E.** Increase in cross-linking of type I and type III collagens associated with volume-overload hypertrophy. *Circ Res* 63: 399-408, 1988.
121. **Ingels NB, Jr.** Myocardial fiber architecture and left ventricular function. *Technol Health Care* 5: 45-52, 1997.
122. **Ingels NB, Jr., Daughters GT, 2nd, Stinson EB, and Alderman EL.** Measurement of midwall myocardial dynamics in intact man by radiography of surgically implanted markers. *Circulation* 52: 859-867, 1975.
123. **Ingels NB, Jr., Hansen DE, Daughters GT, 2nd, Stinson EB, Alderman EL, and Miller DC.** Relation between longitudinal, circumferential, and oblique shortening and torsional deformation in the left ventricle of the transplanted human heart. *Circ Res* 64: 915-927, 1989.
124. **Jackson BM, Gorman JH, 3rd, Salgo IS, Moainie SL, Plappert T, St John-Sutton M, Edmunds LH, Jr., and Gorman RC.** Border zone geometry increases wall stress after myocardial infarction: contrast echocardiographic assessment. *Am J Physiol Heart Circ Physiol* 284: H475-479, 2003.
125. **Jackson BM, Gorman JH, Moainie SL, Guy TS, Narula N, Narula J, John-Sutton MG, Edmunds LH, Jr., and Gorman RC.** Extension of borderzone myocardium in postinfarction dilated cardiomyopathy. *J Am Coll Cardiol* 40: 1160-1167; discussion 1168-1171, 2002.
126. **Janse MJ, Sosunov EA, Coronel R, Opthof T, Anyukhovsky EP, de Bakker JM, Plotnikov AN, Shlapakova IN, Danilo P, Jr., Tijssen JG, and Rosen MR.** Repolarization gradients in the canine left ventricle before and after induction of short-term cardiac memory. *Circulation* 112: 1711-1718, 2005.
127. **Janz RF and Waldron RJ.** Predicted effect of chronic apical aneurysms on the passive stiffness of the human left ventricle. *Circ Res* 42: 255-263, 1978.
128. **Kamkin A, Kiseleva I, and Isenberg G.** Stretch-activated currents in ventricular myocytes: amplitude and arrhythmogenic effects increase with hypertrophy. *Cardiovasc Res* 48: 409-420, 2000.
129. **Karagueuzian HS, Fenoglio JJ, Jr., Weiss MB, and Wit AL.** Protracted ventricular tachycardia induced by premature stimulation of the canine heart after coronary artery occlusion and reperfusion. *Circ Res* 44: 833-846, 1979.
130. **Karlsson MO, Glasson JR, Bolger AF, Daughters GT, Komeda M, Foppiano LE, Miller DC, and Ingels NB, Jr.** Mitral valve opening in the ovine heart. *Am J Physiol* 274: H552-563, 1998.
131. **Kass DA.** Ventricular resynchronization: pathophysiology and identification of responders. *Rev Cardiovasc Med* 4 Suppl 2: S3-S13, 2003.
132. **Kass DA, Bronzwaer JG, and Paulus WJ.** What mechanisms underlie diastolic dysfunction in heart failure? *Circ Res* 94: 1533-1542, 2004.
133. **Kass DA, Chen CH, Curry C, Talbot M, Berger R, Fetis B, and Nevo E.** Improved left ventricular mechanics from acute VDD pacing in patients with dilated cardiomyopathy and ventricular conduction delay. *Circulation* 99: 1567-1573, 1999.
134. **Kellman P, Arai AE, McVeigh ER, and Aletras AH.** Phase-sensitive inversion recovery for detecting myocardial infarction using gadolinium-delayed hyperenhancement. *Magn Reson Med* 47: 372-383, 2002.
135. **Kerber RE, Marcus ML, Ehrhardt J, Wilson R, and Abboud FM.** Correlation between echocardiographically demonstrated segmental dyskinesis and regional myocardial perfusion. *Circulation* 52: 1097-1104, 1975.
136. **Kersschot IE, Brugada P, Ramentol M, Zehender M, Waldecker B, Stevenson WG, Geibel A, De Zwaan C, and Wellens HJ.** Effects of early reperfusion in acute myocardial infarction on arrhythmias induced by programmed stimulation: a prospective, randomized study. *J Am Coll Cardiol* 7: 1234-1242, 1986.
137. **Kim D, Gilson WD, Kramer CM, and Epstein FH.** Myocardial tissue tracking with two-dimensional cine displacement-encoded MR imaging: development and initial evaluation. *Radiology* 230: 862-871, 2004.
138. **Kim RJ, Fieno DS, Parrish TB, Harris K, Chen EL, Simonetti O, Bundy J, Finn JP, Klocke FJ, and Judd RM.** Relationship of MRI delayed contrast enhancement to irreversible injury, infarct age, and contractile function. *Circulation* 100: 1992-2002, 1999.
139. **Kiseleva I, Kamkin A, Wagner KD, Theres H, Ladhoff A, Scholz H, Gunther J, and Lab MJ.** Mechanoelectric feedback after left ventricular infarction in rats. *Cardiovasc Res* 45: 370-378, 2000.
140. **Klein GJ, Ideker RE, Smith WM, Harrison LA, Kasell J, Wallace AG, and Gallagher JJ.** Epicardial mapping of the onset of ventricular tachycardia initiated by programmed stimulation in the canine heart with chronic infarction. *Circulation* 60: 1375-1384, 1979.
141. **Kohl P, Day K, and Noble D.** Cellular mechanisms of cardiac mechano-electric feedback in a mathematical model. *Can J Cardiol* 14: 111-119, 1998.

142. **Kohl P, Nesbitt AD, Cooper PJ, and Lei M.** Sudden cardiac death by Commotio cordis: role of mechano-electric feedback. *Cardiovasc Res* 50: 280-289, 2001.
143. **Kramer CM, Lima JA, Reichek N, Ferrari VA, Llaneras MR, Palmon LC, Yeh IT, Tallant B, and Axel L.** Regional differences in function within noninfarcted myocardium during left ventricular remodeling. *Circulation* 88: 1279-1288, 1993.
144. **Kuijjer JP, Marcus JT, Gotte MJ, van Rossum AC, and Heethaar RM.** Three-dimensional myocardial strains at end-systole and during diastole in the left ventricle of normal humans. *J Cardiovasc Magn Reson* 4: 341-351, 2002.
145. **Kuller L, Lilienfeld A, and Fisher R.** An epidemiological study of sudden and unexpected deaths in adults. *Medicine (Baltimore)* 46: 341-361, 1967.
146. **Lab MJ.** Mechanically dependent changes in action potentials recorded from the intact frog ventricle. *Circ Res* 42: 519-528, 1978.
147. **Leclercq C, Cazeau S, Le Breton H, Ritter P, Mabo P, Gras D, Pavin D, Lazarus A, and Daubert JC.** Acute hemodynamic effects of biventricular DDD pacing in patients with end-stage heart failure. *J Am Coll Cardiol* 32: 1825-1831, 1998.
148. **Leclercq C, Faris O, Tunin R, Johnson J, Kato R, Evans F, Spinelli J, Halperin H, McVeigh E, and Kass DA.** Systolic improvement and mechanical resynchronization does not require electrical synchrony in the dilated failing heart with left bundle-branch block. *Circulation* 106: 1760-1763, 2002.
149. **Lee DS, Green LD, Liu PP, Dorian P, Newman DM, Grant FC, Tu JV, and Alter DA.** Effectiveness of implantable defibrillators for preventing arrhythmic events and death: a meta-analysis. *J Am Coll Cardiol* 41: 1573-1582, 2003.
150. **LeGrice IJ, Smaill BH, Chai LZ, Edgar SG, Gavin JB, and Hunter PJ.** Laminar structure of the heart: ventricular myocyte arrangement and connective tissue architecture in the dog. *Am J Physiol* 269: H571-582, 1995.
151. **LeGrice IJ, Takayama Y, and Covell JW.** Transverse shear along myocardial cleavage planes provides a mechanism for normal systolic wall thickening. *Circ Res* 77: 182-193, 1995.
152. **LeGrice IJ, Takayama Y, Holmes JW, and Covell JW.** Impaired subendocardial function in tachycardia-induced cardiac failure. *Am J Physiol* 268: H1788-1794, 1995.
153. **Lerman BB, Engelstein ED, and Burkhoff D.** Mechanoelectrical feedback: role of beta-adrenergic receptor activation in mediating load-dependent shortening of ventricular action potential and refractoriness. *Circulation* 104: 486-490, 2001.
154. **LeWinter MM, Engler R, and Pavelec RS.** Time-dependent shifts of the left ventricular diastolic filling relationship in conscious dogs. *Circ Res* 45: 641-653, 1979.
155. **Libbus I and Rosenbaum DS.** Transmural action potential changes underlying ventricular electrical remodeling. *J Cardiovasc Electrophysiol* 14: 394-402, 2003.
156. **Lima JA, Becker LC, Melin JA, Lima S, Kallman CA, Weisfeldt ML, and Weiss JL.** Impaired thickening of nonischemic myocardium during acute regional ischemia in the dog. *Circulation* 71: 1048-1059, 1985.
157. **Luu M, Stevenson WG, Stevenson LW, Baron K, and Walden J.** Diverse mechanisms of unexpected cardiac arrest in advanced heart failure. *Circulation* 80: 1675-1680, 1989.
158. **MacKay SA, Potel MJ, and Rubin JM.** Graphics methods for tracking three-dimensional heart wall motion. *Comput Biomed Res* 15: 455-473, 1982.
159. **Maggioni AP, Zuanetti G, Franzosi MG, Rovelli F, Santoro E, Staszewsky L, Tavazzi L, and Tognoni G.** Prevalence and prognostic significance of ventricular arrhythmias after acute myocardial infarction in the fibrinolytic era. GISSI-2 results. *Circulation* 87: 312-322, 1993.
160. **Mahrholdt H, Wagner A, Holly TA, Elliott MD, Bonow RO, Kim RJ, and Judd RM.** Reproducibility of chronic infarct size measurement by contrast-enhanced magnetic resonance imaging. *Circulation* 106: 2322-2327, 2002.
161. **Maier SE, Fischer SE, McKinnon GC, Hess OM, Krayenbuehl HP, and Boesiger P.** Evaluation of left ventricular segmental wall motion in hypertrophic cardiomyopathy with myocardial tagging. *Circulation* 86: 1919-1928, 1992.
162. **Malmivuo J and Plonsey R.** *Bioelectromagnetism-Principles and Applications of Bioelectric and Biomagnetic Fields*. New York: Oxford University Press, 1995.
163. **Mazhari R, Omens JH, Covell JW, and McCulloch AD.** Structural basis of regional dysfunction in acutely ischemic myocardium. *Cardiovasc Res* 47: 284-293, 2000.
164. **McAuliffe MJ, Lalonde FM, McGarry D, Gandler W, Csaky K, and Trus BL.** Medical Image Processing, Analysis & Visualization In Clinical Research. *IEEE Computer-based Medical Systems (CBMS)*: 381-386, 2001.
165. **McCullagh WH, Covell JW, and Ross J, Jr.** Left ventricular dilatation and diastolic compliance changes during chronic volume overloading. *Circulation* 45: 943-951, 1972.

166. McCulloch AD and Omens JH. Non-homogeneous analysis of three-dimensional transmural finite deformation in canine ventricular myocardium. *J Biomech* 24: 539-548, 1991.
167. McCulloch AD, Sung D, Wilson JM, Pavelec RS, and Omens JH. Flow-function relations during graded coronary occlusions in the dog: effects of transmural location and segment orientation. *Cardiovasc Res* 37: 636-645, 1998.
168. McVeigh ER, Prinzen FW, Wyman BT, Tsitlik JE, Halperin HR, and Hunter WC. Imaging asynchronous mechanical activation of the paced heart with tagged MRI. *Magn Reson Med* 39: 507-513, 1998.
169. Medina-Ravell VA, Lankipalli RS, Yan GX, Antzelevitch C, Medina-Malpica NA, Medina-Malpica OA, Droogan C, and Kowey PR. Effect of epicardial or biventricular pacing to prolong QT interval and increase transmural dispersion of repolarization: does resynchronization therapy pose a risk for patients predisposed to long QT or torsade de pointes? *Circulation* 107: 740-746, 2003.
170. Meghji P, Nazir SA, Dick DJ, Bailey ME, Johnson KJ, and Lab MJ. Regional workload induced changes in electrophysiology and immediate early gene expression in intact in situ porcine heart. *J Mol Cell Cardiol* 29: 3147-3155, 1997.
171. Mehta D, Curwin J, Gomes JA, and Fuster V. Sudden death in coronary artery disease: acute ischemia versus myocardial substrate. *Circulation* 96: 3215-3223, 1997.
172. Meier GD, Ziskin MC, Santamore WP, and Bove AA. Kinematics of the beating heart. *IEEE Trans Biomed Eng* 27: 319-329, 1980.
173. Millar CK, Kralios FA, and Lux RL. Correlation between refractory periods and activation-recovery intervals from electrograms: effects of rate and adrenergic interventions. *Circulation* 72: 1372-1379, 1985.
174. Mirsky I and Pasipoularides A. Clinical assessment of diastolic function. *Prog Cardiovasc Dis* 32: 291-318, 1990.
175. Moaveni S. *Finite element analysis: theory and application with ANSYS*. Upper Saddle River, NJ: Prentice Hall, 1999.
176. Moore CC, Lugo-Olivieri CH, McVeigh ER, and Zerhouni EA. Three-dimensional systolic strain patterns in the normal human left ventricle: characterization with tagged MR imaging. *Radiology* 214: 453-466, 2000.
177. Moore CC, O'Dell WG, McVeigh ER, and Zerhouni EA. Calculation of three-dimensional left ventricular strains from biplanar tagged MR images. *J Magn Reson Imaging* 2: 165-175, 1992.
178. Mori S. *Introduction to Diffusion Tensor Imaging*. New York: Elsevier Science, 2007.
179. Myerburg RJ. Sudden cardiac death: exploring the limits of our knowledge. *J Cardiovasc Electrophysiol* 12: 369-381, 2001.
180. Myerburg RJ, Interian A, Jr., Mitrani RM, Kessler KM, and Castellanos A. Frequency of sudden cardiac death and profiles of risk. *Am J Cardiol* 80: 10F-19F, 1997.
181. Myerburg RJ, Kessler KM, and Castellanos A. Sudden cardiac death. Structure, function, and time-dependence of risk. *Circulation* 85: 12-10, 1992.
182. Myerburg RJ, Kessler KM, and Castellanos A. Sudden cardiac death: epidemiology, transient risk, and intervention assessment. *Ann Intern Med* 119: 1187-1197, 1993.
183. Myerburg RJ, Mitrani R, Interian A, Jr., and Castellanos A. Interpretation of outcomes of antiarrhythmic clinical trials: design features and population impact. *Circulation* 97: 1514-1521, 1998.
184. Nagel E, Stuber M, Lakatos M, Scheidegger MB, Boesiger P, and Hess OM. Cardiac rotation and relaxation after anterolateral myocardial infarction. *Coron Artery Dis* 11: 261-267, 2000.
185. Nash MP. *Mechanics and material properties of the heart using an anatomically accurate mathematical model* (Doctor of Philosophy). Auckland: University of Auckland, 1998.
186. Nazarian S, Bluemke DA, Lardo AC, Zviman MM, Watkins SP, Dickfeld TL, Meininger GR, Roguin A, Calkins H, Tomaselli GF, Weiss RG, Berger RD, Lima JA, and Halperin HR. Magnetic resonance assessment of the substrate for inducible ventricular tachycardia in nonischemic cardiomyopathy. *Circulation* 112: 2821-2825, 2005.
187. Nelson GS, Curry CW, Wyman BT, Kramer A, Declerck J, Talbot M, Douglas MR, Berger RD, McVeigh ER, and Kass DA. Predictors of systolic augmentation from left ventricular preexcitation in patients with dilated cardiomyopathy and intraventricular conduction delay. *Circulation* 101: 2703-2709, 2000.
188. Nielsen PM, Le Grice IJ, Smaill BH, and Hunter PJ. Mathematical model of geometry and fibrous structure of the heart. *Am J Physiol* 260: H1365-1378, 1991.
189. Nishimura DG. *Principles of magnetic Resonance Imaging*. Stanford: Stanford University, 1996.
190. Nishimura S, Kawai Y, Nakajima T, Hosoya Y, Fujita H, Katoh M, Yamashita H, Nagai R, and Sugiura S. Membrane potential of rat ventricular myocytes responds to axial stretch in phase, amplitude and speed-dependent manners. *Cardiovasc Res*, 2006.

191. **O'Connell JB and Bristow MR.** Economic impact of heart failure in the United States: time for a different approach. *J Heart Lung Transplant* 13: S107-112, 1994.
192. **O'Dell WG and McCulloch AD.** Imaging three-dimensional cardiac function. *Annu Rev Biomed Eng* 2: 431-456, 2000.
193. **Omens JH and Covell JW.** Transmural distribution of myocardial tissue growth induced by volume-overload hypertrophy in the dog. *Circulation* 84: 1235-1245, 1991.
194. **Ozturk C, Derbyshire JA, and McVeigh ER.** Estimating motion from MRI data. *Proceedings of the IEEE* 91: 1627-1648, 2003.
195. **Poelzing S, Dikshteyn M, and Rosenbaum DS.** Transmural conduction is not a two-way street. *J Cardiovasc Electrophysiol* 16: 455, 2005.
196. **Poelzing S, Roth BJ, and Rosenbaum DS.** Optical measurements reveal nature of intercellular coupling across ventricular wall. *Am J Physiol Heart Circ Physiol* 289: H1428-1435, 2005.
197. **Pouleur H, Rousseau MF, van Eyll C, Brasseur LA, and Charlier AA.** Force-velocity-length relations in hypertrophic cardiomyopathy: evidence of normal or depressed myocardial contractility. *Am J Cardiol* 52: 813-817, 1983.
198. **Prinzen FW, Arts T, Hoeks AP, and Reneman RS.** Discrepancies between myocardial blood flow and fiber shortening in the ischemic border zone as assessed with video mapping of epicardial deformation. *Pflugers Arch* 415: 220-229, 1989.
199. **Prinzen FW, Augustijn CH, Arts T, Allessie MA, and Reneman RS.** Redistribution of myocardial fiber strain and blood flow by asynchronous activation. *Am J Physiol* 259: H300-308, 1990.
200. **Prinzen FW, Hunter WC, Wyman BT, and McVeigh ER.** Mapping of regional myocardial strain and work during ventricular pacing: experimental study using magnetic resonance imaging tagging. *J Am Coll Cardiol* 33: 1735-1742, 1999.
201. **Priori SG, Aliot E, Blomstrom-Lundqvist C, Bossaert L, Breithardt G, Brugada P, Camm AJ, Cappato R, Cobbe SM, Di Mario C, Maron BJ, McKenna WJ, Pedersen AK, Ravens U, Schwartz PJ, Trusz-Gluza M, Vardas P, Wellens HJ, and Zipes DP.** Task Force on Sudden Cardiac Death of the European Society of Cardiology. *Eur Heart J* 22: 1374-1450, 2001.
202. **Rademakers FE, Buchalter MB, Rogers WJ, Zerhouni EA, Weisfeldt ML, Weiss JL, and Shapiro EP.** Dissociation between left ventricular untwisting and filling. Accentuation by catecholamines. *Circulation* 85: 1572-1581, 1992.
203. **Reeder SB, Atalar E, Faranesh AZ, and McVeigh ER.** Multi-echo segmented k-space imaging: an optimized hybrid sequence for ultrafast cardiac imaging. *Magn Reson Med* 41: 375-385, 1999.
204. **Reiter MJ, Synhorst DP, and Mann DE.** Electrophysiological effects of acute ventricular dilatation in the isolated rabbit heart. *Circ Res* 62: 554-562, 1988.
205. **Remme EW, Lyseggen E, Nash MP, Helle-Valle T, Opdahl A, Vartdal T, Pettersen E, Ragnarsson A, Edvardsen T, and Smiseth OA.** Mechanism behind the velocity spike during isovolumic relaxation. *Circulation* 112: U324, 1361, 2005.
206. **Rodriguez EK, Hunter WC, Royce MJ, Leppo MK, Douglas AS, and Weisman HF.** A method to reconstruct myocardial sarcomere lengths and orientations at transmural sites in beating canine hearts. *Am J Physiol* 263: H293-306, 1992.
207. **Ross J, Jr. and McCullagh WH.** Nature of enhanced performance of the dilated left ventricle in the dog during chronic volume overloading. *Circ Res* 30: 549-556, 1972.
208. **Ross J, Jr., Sonnenblick EH, Taylor RR, Spotnitz HM, and Covell JW.** Diastolic geometry and sarcomere lengths in the chronically dilated canine left ventricle. *Circ Res* 28: 49-61, 1971.
209. **Ross RS and Borg TK.** Integrins and the myocardium. *Circ Res* 88: 1112-1119, 2001.
210. **Sakai K, Watanabe K, and Millard RW.** Defining the mechanical border zone: a study in the pig heart. *Am J Physiol* 249: H88-94, 1985.
211. **Sallin EA.** Fiber orientation and ejection fraction in the human left ventricle. *Biophys J* 9: 954-964, 1969.
212. **Santoni-Rugiu F and Gomes JA.** Methods of identifying patients at high risk of subsequent arrhythmic death after myocardial infarction. *Curr Probl Cardiol* 24: 117-160, 1999.
213. **Sasano T, McDonald AD, Kikuchi K, and Donahue JK.** Molecular ablation of ventricular tachycardia after myocardial infarction. *Nat Med*, 2006.
214. **Saxon LA, Kerwin WF, Cahalan MK, Kalman JM, Olgin JE, Foster E, Schiller NB, Shinbane JS, Lesh MD, and Merrick SH.** Acute effects of intraoperative multisite ventricular pacing on left ventricular function and activation/contraction sequence in patients with depressed ventricular function. *J Cardiovasc Electrophysiol* 9: 13-21, 1998.

215. **Sengupta PP, Khandheria BK, Korinek J, Wang J, and Belohlavek M.** Biphasic tissue Doppler waveforms during isovolumic phases are associated with asynchronous deformation of subendocardial and subepicardial layers. *J Appl Physiol* 99: 1104-1111, 2005.
216. **Sengupta PP, Khandheria BK, Korinek J, Wang J, Jahangir A, Seward JB, and Belohlavek M.** Apex-to-base dispersion in regional timing of left ventricular shortening and lengthening. *J Am Coll Cardiol* 47: 163-172, 2006.
217. **Sicouri S and Antzelevitch C.** A subpopulation of cells with unique electrophysiological properties in the deep subepicardium of the canine ventricle. The M cell. *Circ Res* 68: 1729-1741, 1991.
218. **Smaill BH, LeGrice IJ, Hooks DA, Pullan AJ, Caldwell BJ, and Hunter PJ.** Cardiac structure and electrical activation: models and measurement. *Clin Exp Pharmacol Physiol* 31: 913-919, 2004.
219. **Smith VE and Zile MR.** Relaxation and diastolic properties of the heart. In: *The Heart and Cardiovascular System*, edited by Fozzart HA et al. New York, NY: Raven Press, 1992, p. 1353-1367.
220. **Solomon SD, Zelenkofske S, McMurray JJ, Finn PV, Velazquez E, Ertl G, Harsanyi A, Rouleau JL, Maggioni A, Kober L, White H, Van de Werf F, Pieper K, Califf RM, and Pfeffer MA.** Sudden death in patients with myocardial infarction and left ventricular dysfunction, heart failure, or both. *N Engl J Med* 352: 2581-2588, 2005.
221. **Spach MS and Barr RC.** Ventricular intramural and epicardial potential distributions during ventricular activation and repolarization in the intact dog. *Circ Res* 37: 243-257, 1975.
222. **Spotnitz HM, Spotnitz WD, Cottrell TS, Spiro D, and Sonnenblick EH.** Cellular basis for volume related wall thickness changes in the rat left ventricle. *J Mol Cell Cardiol* 6: 317-331, 1974.
223. **Stejskal EO.** Use of spin echos in a pulsed magnetic field gradient to study anisotropic, restricted diffusion and flow. *J Chem Phys* 43: 3597-3603, 1965.
224. **Stevenson WG and Soejima K.** Recording techniques for clinical electrophysiology. *J Cardiovasc Electrophysiol* 16: 1017-1022, 2005.
225. **Streeter DD, Jr., Spotnitz HM, Patel DP, Ross J, Jr., and Sonnenblick EH.** Fiber orientation in the canine left ventricle during diastole and systole. *Circ Res* 24: 339-347, 1969.
226. **Stuber M, Scheidegger MB, Fischer SE, Nagel E, Steinemann F, Hess OM, and Boesiger P.** Alterations in the local myocardial motion pattern in patients suffering from pressure overload due to aortic stenosis. *Circulation* 100: 361-368, 1999.
227. **Sung D, Mills RW, Schettler J, Narayan SM, Omens JH, and McCulloch AD.** Ventricular filling slows epicardial conduction and increases action potential duration in an optical mapping study of the isolated rabbit heart. *J Cardiovasc Electrophysiol* 14: 739-749, 2003.
228. **Taggart P, Sutton P, Opthof T, Coronel R, and Kallis P.** Electrotonic cancellation of transmural electrical gradients in the left ventricle in man. *Prog Biophys Mol Biol* 82: 243-254, 2003.
229. **Taggart P and Sutton PM.** Cardiac mechano-electric feedback in man: clinical relevance. *Prog Biophys Mol Biol* 71: 139-154, 1999.
230. **Takayama Y, Costa KD, and Covell JW.** Contribution of laminar myofiber architecture to load-dependent changes in mechanics of LV myocardium. *Am J Physiol Heart Circ Physiol* 282: H1510-1520, 2002.
231. **Taylor RR, Covell JW, and Ross JJ.** Left ventricular function in experimental aorto-caval fistula with circulatory congestion and fluid retention. *J Clin Invest* 47: 1333-1342, 1968.
232. **Tibayan FA, Lai DT, Timek TA, Dagum P, Liang D, Daughters GT, Ingels NB, and Miller DC.** Alterations in left ventricular torsion in tachycardia-induced dilated cardiomyopathy. *J Thorac Cardiovasc Surg* 124: 43-49, 2002.
233. **Torrent-Guasp F, Kocica MJ, Corno AF, Komeda M, Carreras-Costa F, Flotats A, Cosin-Aguillar J, and Wen H.** Towards new understanding of the heart structure and function. *Eur J Cardiothorac Surg* 27: 191-201, 2005.
234. **Tseng WY, Wedeen VJ, Reese TG, Smith RN, and Halpern EF.** Diffusion tensor MRI of myocardial fibers and sheets: Correspondence with visible cut-face texture. *J Magn Reson Imaging* 17: 31-42, 2003.
235. **Ursell PC, Gardner PI, Albala A, Fenoglio JJ, Jr., and Wit AL.** Structural and electrophysiological changes in the epicardial border zone of canine myocardial infarcts during infarct healing. *Circ Res* 56: 436-451, 1985.
236. **van Dam RT and Durrer D.** Experimental study on the intramural distribution of the excitability cycle and on the form of the epicardial T wave in the dog heart in situ. *Am Heart J* 61: 537-542, 1961.
237. **van Dam RT and Durrer D.** The T wave and ventricular repolarization. *Am J Cardiol* 14: 294-300, 1964.
238. **Van Leuven SL, Waldman LK, McCulloch AD, and Covell JW.** Gradients of epicardial strain across the perfusion boundary during acute myocardial ischemia. *Am J Physiol* 267: H2348-2362, 1994.
239. **Vasan RS, Benjamin EJ, and Levy D.** Prevalence, clinical features and prognosis of diastolic heart failure: an epidemiologic perspective. *J Am Coll Cardiol* 26: 1565-1574, 1995.

240. **Vasan RS and Levy D.** Defining diastolic heart failure: a call for standardized diagnostic criteria. *Circulation* 101: 2118-2121, 2000.
241. **Voigt JU, Lindenmeier G, Exner B, Regenfus M, Werner D, Reulbach U, Nixdorff U, Flachskampf FA, and Daniel WG.** Incidence and characteristics of segmental postsystolic longitudinal shortening in normal, acutely ischemic, and scarred myocardium. *J Am Soc Echocardiogr* 16: 415-423, 2003.
242. **von Segesser LK.** The myocardial band: fiction or fact? *Eur J Cardiothorac Surg* 27: 181-182, 2005.
243. **Wagner A, Mahrholdt H, Holly TA, Elliott MD, Regenfus M, Parker M, Klocke FJ, Bonow RO, Kim RJ, and Judd RM.** Contrast-enhanced MRI and routine single photon emission computed tomography (SPECT) perfusion imaging for detection of subendocardial myocardial infarcts: an imaging study. *Lancet* 361: 374-379, 2003.
244. **Waldman LK and Covell JW.** Effects of ventricular pacing on finite deformation in canine left ventricles. *Am J Physiol* 252: H1023-1030, 1987.
245. **Waldman LK, Fung YC, and Covell JW.** Transmural myocardial deformation in the canine left ventricle. Normal in vivo three-dimensional finite strains. *Circ Res* 57: 152-163, 1985.
246. **Waldman LK, Nosan D, Villarreal F, and Covell JW.** Relation between transmural deformation and local myofiber direction in canine left ventricle. *Circ Res* 63: 550-562, 1988.
247. **Weiss JL, Frederiksen JW, and Weisfeldt ML.** Hemodynamic determinants of the time-course of fall in canine left ventricular pressure. *J Clin Invest* 58: 751-760, 1976.
248. **Wetstein L, Mark R, Kaplinsky E, Mitamura H, Kaplan A, Sauermelch C, and Michelson EL.** Histopathologic factors conducive to experimental ventricular tachycardia. *Surgery* 98: 532-539, 1985.
249. **Wilkoff BL, Cook JR, Epstein AE, Greene HL, Hallstrom AP, Hsia H, Kutalek SP, and Sharma A.** Dual-chamber pacing or ventricular backup pacing in patients with an implantable defibrillator: the Dual Chamber and VVI Implantable Defibrillator (DAVID) Trial. *Jama* 288: 3115-3123, 2002.
250. **Wit AL and Janse MJ.** Experimental models of ventricular tachycardia and fibrillation caused by ischemia and infarction. *Circulation* 85: 132-42, 1992.
251. **Wyman BT, Hunter WC, Prinzen FW, Faris OP, and McVeigh ER.** Effects of single- and biventricular pacing on temporal and spatial dynamics of ventricular contraction. *Am J Physiol Heart Circ Physiol* 282: H372-379, 2002.
252. **Wyman BT, Hunter WC, Prinzen FW, and McVeigh ER.** Mapping propagation of mechanical activation in the paced heart with MRI tagging. *Am J Physiol* 276: H881-891, 1999.
253. **Yan GX and Antzelevitch C.** Cellular basis for the Brugada syndrome and other mechanisms of arrhythmogenesis associated with ST-segment elevation. *Circulation* 100: 1660-1666, 1999.
254. **Yan GX and Antzelevitch C.** Cellular basis for the normal T wave and the electrocardiographic manifestations of the long-QT syndrome. *Circulation* 98: 1928-1936, 1998.
255. **Yasuda S, Sugiura S, Yamashita H, Nishimura S, Saeki Y, Momomura S, Katoh K, Nagai R, and Sugi H.** Unloaded shortening increases peak of Ca²⁺ transients but accelerates their decay in rat single cardiac myocytes. *Am J Physiol Heart Circ Physiol* 285: H470-475, 2003.
256. **Yellin EL and Meisner JS.** Physiology of diastolic function and transmitral pressure-flow relations. *Cardiol Clin* 18: 411-433, vii, 2000.
257. **Yoran C, Covell JW, and Ross J, Jr.** Rapid fixation of the left ventricle: continuous angiographic and dynamic recordings. *J Appl Physiol* 35: 155-157, 1973.
258. **Young AA, Kramer CM, Ferrari VA, Axel L, and Reichek N.** Three-dimensional left ventricular deformation in hypertrophic cardiomyopathy. *Circulation* 90: 854-867, 1994.
259. **Yue AM, Betts TR, Roberts PR, and Morgan JM.** Global dynamic coupling of activation and repolarization in the human ventricle. *Circulation* 112: 2592-2601, 2005.
260. **Yun KL, Niczyporuk MA, Daughters GT, 2nd, Ingels NB, Jr., Stinson EB, Alderman EL, Hansen DE, and Miller DC.** Alterations in left ventricular diastolic twist mechanics during acute human cardiac allograft rejection. *Circulation* 83: 962-973, 1991.
261. **Zabel M, Koller BS, Sachs F, and Franz MR.** Stretch-induced voltage changes in the isolated beating heart: importance of the timing of stretch and implications for stretch-activated ion channels. *Cardiovasc Res* 32: 120-130, 1996.
262. **Zabel M, Portnoy S, and Franz MR.** Effect of sustained load on dispersion of ventricular repolarization and conduction time in the isolated intact rabbit heart. *J Cardiovasc Electrophysiol* 7: 9-16, 1996.
263. **Zeng T, Bett GC, and Sachs F.** Stretch-activated whole cell currents in adult rat cardiac myocytes. *Am J Physiol Heart Circ Physiol* 278: H548-557, 2000.
264. **Zerhouni EA, Parish DM, Rogers WJ, Yang A, and Shapiro EP.** Human heart: tagging with MR imaging--a method for noninvasive assessment of myocardial motion. *Radiology* 169: 59-63, 1988.
265. **Zheng ZJ, Croft JB, Giles WH, and Mensah GA.** Sudden cardiac death in the United States, 1989 to 1998. *Circulation* 104: 2158-2163, 2001.

266. **Zile MR, Baicu CF, and Gaasch WH.** Diastolic heart failure--abnormalities in active relaxation and passive stiffness of the left ventricle. *N Engl J Med* 350: 1953-1959, 2004.
267. **Zile MR and Brutsaert DL.** New concepts in diastolic dysfunction and diastolic heart failure: Part I: diagnosis, prognosis, and measurements of diastolic function. *Circulation* 105: 1387-1393, 2002.
268. **Zile MR and Brutsaert DL.** New concepts in diastolic dysfunction and diastolic heart failure: Part II: causal mechanisms and treatment. *Circulation* 105: 1503-1508, 2002.
269. **Zipes DP, Camm AJ, Borggrefe M, Buxton AE, Chaitman B, Fromer M, Gregoratos G, Klein G, Moss AJ, Myerburg RJ, Priori SG, Quinones MA, Roden DM, Silka MJ, Tracy C, Smith SC, Jr., Jacobs AK, Adams CD, Antman EM, Anderson JL, Hunt SA, Halperin JL, Nishimura R, Ornato JP, Page RL, Riegel B, Blanc JJ, Budaj A, Dean V, Deckers JW, Despres C, Dickstein K, Lekakis J, McGregor K, Metra M, Morais J, Osterspey A, Tamargo JL, and Zamorano JL.** ACC/AHA/ESC 2006 Guidelines for Management of Patients With Ventricular Arrhythmias and the Prevention of Sudden Cardiac Death: a report of the American College of Cardiology/American Heart Association Task Force and the European Society of Cardiology Committee for Practice Guidelines (writing committee to develop Guidelines for Management of Patients With Ventricular Arrhythmias and the Prevention of Sudden Cardiac Death): developed in collaboration with the European Heart Rhythm Association and the Heart Rhythm Society. *Circulation* 114: e385-484, 2006.
270. **Zipes DP and Wellens HJ.** Sudden cardiac death. *Circulation* 98: 2334-2351, 1998.
271. **Zwanenburg JJ, Gotte MJ, Kuijer JP, Heethaar RM, van Rossum AC, and Marcus JT.** Timing of cardiac contraction in humans mapped by high-temporal-resolution MRI tagging: early onset and late peak of shortening in lateral wall. *Am J Physiol Heart Circ Physiol* 286: H1872-1880, 2004.
272. **Zwanenburg JJ, Gotte MJ, Kuijer JP, Hofman MB, Knaapen P, Heethaar RM, van Rossum AC, and Marcus JT.** Regional timing of myocardial shortening is related to prestretch from atrial contraction: assessment by high temporal resolution MRI tagging in humans. *Am J Physiol Heart Circ Physiol* 288: H787-794, 2005.

Acknowledgement

This thesis completes my journey over the past 5 years. When I look back, I can only remember good days. However, the path was often difficult to find, and I was just fortunate enough to find a handful of excellent and brilliant people around me who guided me to make my way through darkness.

First and foremost, I thank James W. Covell, MD at the University of California, San Diego (UCSD) for introducing me to the world of science. A superb scientist, surgeon, physiologist, engineer, and fisherman, Jim taught me the excitement and fun of doing science. I will never forget the exciting moments of large animal experiments in his laboratory. Jim also gave me an opportunity to work with excellent people in and out of his group: Jeffrey H. Omens, PhD, Andrew D. McCulloch, PhD, Rish Pavelec, and Rachel Alexander at UCSD, Neil B. Ingels, PhD and D. Craig Miller, MD at Stanford University, and John C. Criscione, MD, PhD at Texas A&M University. I feel indebted to Kirk U. Knowlton, MD, the former fellowship program director, and at present Chief of Cardiology at UCSD, for always going out of his way to support me. I am also grateful to the American Heart Association, the Western States Affiliate, for supporting my research during this period.

Second, I thank Elliot R. McVeigh, PhD and the “*critical mass of smart people*” in his group at the National Heart, Lung and Blood Institute. Under Elliot’s unique and excellent leadership that fosters independence, his laboratory is always filled with exceptional individuals with keen intellect and playful mind, including J. Andrew Derbyshire, PhD, Steven R. Mickelsen, MD, Bruce Hopenfeld, PhD, Daniel B. Ennis, PhD, Daniel A. Herzka, PhD, Reza Nezafat, PhD, Luis F Gutiérrez, PhD and Peter Kellman, PhD. I also feel grateful to Han Wen, PhD and Ignacio Rodriguez, PhD for their technical help. I thank the staff at the Laboratory of Cardiac Energetics and the Laboratory of Animal Medicine and Surgery for excellent surgical assistance: Joni Taylor, Katie Hope, Kathy Lucas, Robert F. Hoyt, Jr., DVM, Randy Clevenger, Dave Caden, Arthur Zetts, Kenneth Jeffries, Gayle Zywicke, Karen Keeran, and Shawn Kozlov.

Third, I thank Henry R. Halperin, MD, MA, Timm Dickfeld, MD, PhD, and Z. Muz Zviman, PhD at the Johns Hopkins University School of Medicine for their critical input and help on the aspect of cardiac electrophysiology of my research. Henry, a tough-minded optimist, has always been a source of great inspiration.

Forth, I thank Ryoza Nagai, MD, PhD and the collaborators at the University of Tokyo School of Medicine: Tomohiko Masumoto, MD, PhD and Kohsuke Ajiki, MD. Ryoza, my thesis advisor, gave me an opportunity to write this thesis as a compendium of my work in the field of cardiac electromechanics. I am also grateful to Masao Omata, MD and Takanobu Tomaru, MD for introducing me to the path of a physician-scientist.

Lastly, I thank my wife Satoko for her constant love and support, without which my life wouldn’t mean as much.

H.A.

January 2007

List of Abbreviations and Acronyms

AF	atrial fibrillation
ANOVA	analysis of variance
AoP	aortic pressure
APD	action potential duration
ARI	activation-recovery interval
AV	atrioventricular
bpm	beats per minute
BW	bandwidth
CHD	coronary heart disease
CL	cycle length
CRT	cardiac resynchronization therapy
DENSE	displacement encoding of stimulated echo
EC	early contraction
ECG	electrocardiogram
ECM	extracellular matrix
ED	End diastole
EDP	End-diastolic pressure
EDV	End-diastolic volume
EF	ejection fraction
EPI	echoplaner imaging
FOV	field of view
Gd-DTPA	Gadolinium diethylene triamine pentaacetate
GRE	gradient recalled echo
ICD	implantable cardioverter-defibrillator
IHD	ischemic heart disease
IVC	isovolumic contraction
IVR	isovolumic relaxation
LA	left atrium
LAA	left atrial appendage
LAD	left anterior descending coronary artery
LAP	left atrial pressure
LBBS	left bundle branch block
LCx	left circumflex coronary artery
LV	left ventricle
LVP	left ventricular pressure
MEF	mechanoelectrical feedback
MI	myocardial infarction
MRI	magnetic resonance imaging
MVO	mitral valve opening
PES	programmed electrical stimulation

PPR	peak prestretch rate
PS	peak shortening
PSR	peak shortening rate
RV	right ventricle
RVOT	right ventricular outflow tract
SAC	stretch-activated channel
SCD	sudden cardiac death
SD	standard deviation
SNR	signal-to-noise ratio
SSFP	steady state free precession
TdP	torsade de pointes
TDR	transmural dispersion of repolarization
TDRelax	transmural dispersion of myofiber relaxation
TDSHORT	transmural dispersion of myofiber shortening
TE	echo time
TR	repetition time
TTOS	time to onset of shortening
TTPS	time to peak shortening
VF	ventricular fibrillation
VT	ventricular tachycardia

List of Figures and Tables

Chapter 2

Sudden cardiac death

Figure 2-1. Major implantable cardioverter-defibrillator (ICD) trials. Hazard ratios (vertical line) and 95% confidence intervals (horizontal lines) for death from any cause in the ICD group compared with the non-ICD group. *Includes only ICD and amiodarone patients from CASH. AVID = Antiarrhythmics Versus Implantable Defibrillators; CASH = Cardiac Arrest Study Hamburg; CIDS = Canadian Implantable Defibrillator Study; EF = ejection fraction; HF = heart failure; MADIT = Multicenter Automatic Defibrillator Implantation Trial; MUSTT = Multicenter UnSustained Tachycardia Trial; SCD-HeFT = Sudden Cardiac Death in Heart Failure Trial; CABG = coronary artery bypass graft surgery; EP = electrophysiological study; LVD = left ventricular dysfunction; MI = myocardial infarction; N = number of patients; NICM = nonischemic cardiomyopathy; NSVT = nonsustained ventricular tachycardia; PVCs = premature ventricular complexes; SAECG = signal-averaged electrocardiogram.

Figure 2-2. Absolute numbers of events and event rates of SCD in the general population and in specific subpopulations over 1 year. General population refers to unselected population age greater than or equal to 35 y, and high-risk subgroups to those with multiple risk factors for a first coronary event. Clinical trials that include specific subpopulations of patients are shown in the right side of the figure.

Chapter 3

Cardiac electromechanics

Figure 3-1. Fiber orientation and ejection fraction in a cylindrical LV model.

Figure 3-2. Transmural fiber orientation.

Figure 3-3. Transmural fiber structure. Combination of spiral and circumferential fibers 1) generates large EF (>60%), 2) generates physiological LV pressures, 3) minimizes global LV torsional deformation, and 4) equalizes transmural fiber strain and stress.

Figure 3-4. Systolic shearing of fibers along cleavage planes.

Figure 3-5. Laminar sheet structure.

Figure 3-6. Sheet shear and extension allow systolic wall thickening of >40%. Each circle represents a cross-section of myofiber. X_n , direction normal to the sheet; X_s , sheet direction; X_3 , radial direction; β , sheet angle; E_{sn} , sheet shear; E_{ss} , sheet extension.

Figure 3-7. Cardiac action potential.

Figure 3-8. 3-D isochronic representation of the activation of the human heart. Zero time is the beginning of the LV potential.

Figure 3-9. The deformation gradient tensor, F , carries line segment $d\vec{X}$ into $d\vec{x}$.

Figure 3-10. a) Five reference markers (apex bead, base bead and three epicardial beads) used to calculate a cardiac coordinate system, **b)** The 3-D coordinates of three columns of markers from in the reference coordinate system, **c)** Two projection views of the marker set to calculate the 3-D coordinates

Figure 3-11. Two projection views of the high-speed cineradiographic images. AP, anteroposterior view; LAT, lateral view.

Figure 3-12. A local cardiac coordinate system defined by the transmural bead set. \vec{R} , radial axis; \vec{L} , longitudinal axis; \vec{C} , circumferential axis. Note $\vec{C} = \vec{L} \times \vec{R}$.

Figure 3-13. Relationship between the local cardiac coordinate axes (X_1, X_2, X_3) and the local fiber-sheet coordinate axes (X_s, X_s, X_n).

Figure 3-14. A local fiber-sheet coordinate system and its major strain components.

Figure 3-15. Encoding of the initial location by the first gradient pulse. A circle and an arrow represent a sample and its phase at each time point, respectively.

Figure 3-16. A pair of dephasing (G) and rephasing ($-G$) gradient pulses to encode the displacement of each sample from the initial location.

Figure 3-17. Pulsed gradient stimulated echo (PGSTE) sequence, which stores one component of the magnetization along longitudinal magnetization.

Figure 3-18. Pulse sequence diagram for cine-DENSE. Following an ECG trigger, the dephasing gradient pulse is emitted to encode displacement. A segmented fast gradient-echo echo-planar imaging sequence modified to include the DENSE unencoding (= rephrasing) gradient is used to rapidly sample the displacement-encoded longitudinal magnetization at multiple cardiac phases. G_{RO} = readout gradient, Rf = radiofrequency.

Figure 3-19. Schematic demonstrates the computation of 2D displacement maps from raw data obtained with cine DENSE MR imaging. Complementary data are subtracted to suppress the T_1 relaxation echo, and a small circular filter is applied to remove residual signal. After 2D inverse Fourier transformation (2DIFT), phase correction and phase unwrapping are performed, followed by computation of one-dimensional displacement values. Vector addition of orthogonal

one-dimensional displacement values yields a 2D displacement map. *Phase ref.* = phase reference.

Chapter 4

Regional mechanics during relaxation in normal heart

Figure 4-1. Sites of marker implantation. A: Schematic representation of the heart. X_1 : circumferential axis, X_2 : longitudinal axis, X_3 : radial axis, LAA: left atrial appendage, RCA: right coronary artery, LAD: left anterior descending, D_1 , D_2 : first and second diagonal branch of LAD, respectively. B: Schematic representation of excised tissue block containing the bead set. Fiber angle (α) was measured in the circumferential-longitudinal (X_1 - X_2) plane at each transmural depth with reference to the positive circumferential axis (X_1), with a positive angle defined as rotation towards the longitudinal axis (X_2). Sheet angle (β) was measured in the plane perpendicular to the fiber angle at each transmural depth with reference to the radial axis (X_3), with a positive angle defined as rotation towards the positive crossfiber direction (X_{cf}). X_f : fiber axis, X_s : sheet axis, X_n : axis oriented normal to the sheet plane. The X_f , X_s , and X_n axes present a Cartesian system (See text for details).

Figure 4-2. Early relaxation. Early relaxation was defined as the period beginning at end-systole (ES) and ending at minimum LV pressure (LVP, solid line). White squares represent circumferential strain (E_{11}) at midwall.

Figure 4-3. Measured fiber (α) and sheet (β) angles vs. % wall depth ($n = 5$, mean \pm SE). The mean fiber angles (α) ranged approximately from -60° to $+60^\circ$, from epicardium to endocardium, resulting in a transmural gradient of $\sim 120^\circ$. The mean sheet angles (β) were predominantly negative with small variations across the wall ($-36^\circ \sim -2^\circ$). epi: epicardium, endo: endocardium.

Figure 4-4. Time course of finite strains during early relaxation in local cardiac coordinates. Note significant endocardial circumferential stretch (E_{11}), endocardial wall thinning (E_{33}), epicardial torsional recoil (E_{12}), transverse shear (E_{23} , E_{13}) during early relaxation ($P < 0.05$). Values are means \pm SE. epi: epicardium, mid: midwall, endo: endocardium, ER: early relaxation. ES (end-systole, time = 0%), End of ER (time = 100%). Note different scales for each strain.

Table 4-1. Two-factor repeated measures analysis of variance during early relaxation. Values for epicardial (Epi) and endocardial (Endo) strains are means \pm SE. Statistically significant ($P < 0.05$) effects of time (\star), depth (\dagger), and interaction between time and depth (\ddagger) are shown.

Figure 4-5. Time course of finite strains during early relaxation in fiber-sheet coordinates. Note significant epicardial stretch along the fiber direction (E_{ff}), endocardial sheet shortening (E_{ss}), fiber shear (E_{fs} , E_{fn}) during early relaxation ($P < 0.05$). Values are means \pm SE. epi: epicardium, mid: midwall, endo: endocardium, ER: early relaxation. ES (end-systole, time = 0%), End of ER (time = 100%). Note different scales for each strain.

Chapter 5

Regional mechanics during relaxation in hypertrophied heart

Figure 5-1. A. Schematic representation of the heart. X_1 : circumferential axis, X_2 : longitudinal axis, X_3 : radial axis, LAD: left anterior descending coronary artery, LCx: left circumflex coronary artery, LV: left ventricle, LA: left atrium. A precalibrated micromanometer pressure catheter was inserted into apex to monitor LV pressure. A 9-Fr silicone catheter was inserted into LA to monitor LA pressure, which was used in every imaging study to correct for baseline drifting of the LV micromanometer. **B. Bead set** consisted of three transmural columns of 4-6 gold beads (0.8mm) and a surface gold bead (1.7mm) above each column. Finite deformation of the myocardium was calculated from displacement of each material point (= bead) in space. **C. Diastolic filling.** ECG: surface electrocardiogram, LVP: left ventricular pressure, LAP: left atrial pressure. Diastolic filling was defined as the period beginning at mitral valve opening (time=0%, pressure crossover of LVP and LAP) and ending at end diastole (time=100%, peak of ECG R-wave). White squares in the figure represent longitudinal strain (E_{22}) at 80% wall depth in a control animal. **D. Fiber-sheet coordinate system.** Each cylinder represents a myofiber. Myofibers are organized into laminar “sheets”, which are approximately four cells thick and roughly stacked from apex to base (150). Sheet angle (β) is measured with reference to the positive radial axis (X_3).

Figure 5-2. Illustrative account of fiber (α) and sheet (β) angle measurement. A transmural rectangular block of tissue in the implanted bead set was carefully removed from the ventricular wall, with the edges of the block cut parallel to the local circumferential (X_1), longitudinal (X_2) and radial (X_3) axes of the LV. The block was sliced into 1mm-thick sections parallel to the epicardial tangent plane. In each 1mm-slice tissue, fiber angle (α) was measured with reference to the positive circumferential axis (X_1). Note the orientation of the fiber axis (X_f) rotates counterclockwise from epicardium to endocardium. The 1mm-slice tissue was sectioned perpendicular to the mean fiber direction, and sheet angle (β) was measured in the section plane with reference to the positive radial axis (X_3). This process was repeated in all the 1mm-slice tissues from the epicardium (Epi) to the endocardium (Endo). X_s : sheet axis.

Table 5-1. Hemodynamic parameters. Values are means \pm SE (n=6). LVP_{max} : maximum left ventricular pressure, MVO: mitral valve opening, LVEDP: left ventricular end-diastolic pressure, dP/dt_{max} , dP/dt_{min} : peak positive and negative dP/dt , respectively, τ : time constant of isovolumic LV pressure decline, fiber strain: E_{ff} , sheet strain: E_{ss} , sheet shear: E_{sn} .

Figure 5-3. Transmural fiber and sheet angles during diastolic filling. Values are means \pm SE (n=6). Closed square: mitral valve opening, open square: end diastole, Epi: epicardial surface, Endo: endocardium. Both in control and hypertrophy, transmural fiber angles did not significantly change from mitral valve opening to end diastole ($P=n.s.$). Similarly, transmural sheet angles did not change during diastolic filling in control ($P=n.s.$). In contrast, transmural sheet angles significantly decreased from mitral valve opening to end diastole in hypertrophy (*: $P<0.05$). See text for details.

Figure 5-4. Direction of sheet angle change during diastolic filling. Endo: endocardium, epi: epicardium, X_3 : radial axis, β_{MVO} , β_{ED} : sheet angle at mitral valve opening (MVO) and end diastole (ED), respectively. Because transmural sheet angles were negative at MVO, a decrease

in sheet angle during diastolic filling (Figure 6-2) indicates that the sheets become more oblique to the radial axis towards ED.

Figure 5-5. Cardiac strain time course during diastolic filling in control. Values are means \pm SE (n=6). Epi, endo: 20%, 80% wall depth from the epicardial surface, respectively. MVO: mitral valve opening, ED: end diastole.

Figure 5-6. Fiber-sheet strain time course during diastolic filling. In A, the reference configuration for both control and hypertrophy was determined at the end diastole of the control study. In B, the reference configuration for control and hypertrophy was determined at the end diastole of the control and hypertrophic state, respectively. Values are means \pm SE (n=6). Fiber strain: E_{ff} , sheet strain: E_{ss} , sheet shear: E_{sn} . Epi, endo: 20%, 80% wall depth from the epicardial surface, respectively. MVO: mitral valve opening, ED: end diastole. Closed circle: control, open circle: hypertrophy. *: $P < 0.05$ by two-factor repeated measures ANOVA (control vs. hypertrophy).

Table 5-2. End-systolic strains.

Figure 5-7. Schematic representation of fiber-sheet strains during diastolic filling. A: control, B: hypertrophy. β_{ED} is not significantly different between control ($\beta_{ED-control}$) and hypertrophy ($\beta_{ED-hypertrophy}$). In contrast, β_{MVO} is greater in control ($\beta_{MVO-control}$) than in hypertrophy ($\beta_{MVO-hypertrophy}$). The net result is a significantly greater sheet shear (E_{sn}), which contributes to greater wall thinning, during diastolic filling in hypertrophy than in control. Fiber stretch: E_{ff} , sheet shortening: E_{ss} , MVO: mitral valve opening, ED: end diastole.

Chapter 6

Regional electromechanics in normal heart

Figure 6-1. Schematic representation of the heart. The transmural bead set was implanted between the first (D_1) and the second (D_2) diagonal branch of the left anterior descending coronary artery (LAD) to measure finite deformation of the myocardial tissue across the wall. Epi, epicardium; Endo, endocardium; LV, left ventricle; LCx, left circumflex coronary artery.

Table 6-1. Hemodynamic parameters. Values are mean \pm SD (n=14). LVP_{max} , maximum left ventricular pressure; dP/dt , first derivative of pressure over time; dP/dt_{max} , peak positive dP/dt ; dP/dt_{min} , peak negative dP/dt .

Figure 6-2. Transmural fiber orientation. Values are mean \pm SD (n=14). Fiber angles were measured with reference to the positive circumferential direction. Epi, epicardium; Endo, endocardium.

Figure 6-3. Time course of transmural fiber strains. A. Entire cardiac cycle. Different colors represent the percent wall depth from the epicardial surface. Open circles, the onset of myofiber shortening; open squares, the onset of myofiber relaxation; TDSshort, transmural dispersion of myofiber shortening; TDRelax, transmural dispersion of myofiber relaxation; ECG, electrocardiogram; AoP, central aortic pressure; LVP, left ventricular pressure; LAP, left atrial pressure. B. A closer look at TDSshort. C. A closer look at TDRelax.

Figure 6-4. Transmural dispersion of myofiber mechanics. Values are mean and error bars indicate SD (n=14). Open circles, the onset of myofiber shortening; open squares, the onset of myofiber relaxation; TDS_{Short}, transmural dispersion of myofiber shortening; TDS_{Relax}, transmural dispersion of myofiber relaxation.

Figure 6-5. Bipolar electrograms from plunge electrodes. Red and blue dots mark the time points of steepest portion of initial bipolar QRS waveforms and end of T-wave, respectively. Note the endocardial-to-epicardial direction of depolarization, whereas no clear transmural dispersion of repolarization is observed.

Figure 6-6. Electrical activation (open triangles) and the onset of myofiber shortening (open circles) vs. mean wall depth. The open triangles represent the electrical activation (n=4) mean value at each depth (mm). The open circles represent the onset of myofiber shortening (n=14) mean value at each depth (mm).

Figure 6-7. Electrical repolarization (closed triangles) and the onset of myofiber relaxation (open squares) vs. mean wall depth. The closed triangles represent the electrical repolarization (n=4) mean value at each depth (mm). The open squares represent the onset of myofiber shortening (n=14) mean value at each depth (mm).

Figure 6-8. Transmural tissue coupling. Purple and green lines indicate strains in epicardial (0% wall depth) and endocardial (90% wall depth) layers, respectively. Solid and broken lines indicate fiber and cross-fiber strains, respectively. IVC, isovolumic contraction; IVR, isovolumic relaxation.

Chapter 7

Regional electromechanics in paced heart

Figure 7-1. A: Schematic representation of the left ventricle. X_1 : circumferential axis, X_2 : longitudinal axis, X_3 : radial axis, LAD: left anterior descending coronary artery, D_1 , D_2 : first and second diagonal branch of LAD, respectively. **B: Schematic representation of local fiber-sheet axes.** Fiber angle (α) was measured in the circumferential-longitudinal (X_1 - X_2) plane at each wall depth with reference to the positive circumferential axis (X_1). Sheet angle (β) was measured in the plane perpendicular to the fiber angle at each wall depth with reference to the radial axis (X_3). X_f : fiber axis, X_s : sheet axis, X_n : axis oriented normal to the sheet plane. The X_f , X_s , and X_n axes present a Cartesian system (For details, see (17)).

Figure 7-2. Three cardiac phases. EC: early contraction phase, Ejection: ejection phase, ER: early relaxation phase, ED: end-diastole, ES: end-systole, LVP_{min} : minimum LV pressure.

Table 7-1. Hemodynamic parameters and time intervals. Values are means \pm SE (n=5). LV: left ventricle, dP/dt_{max} : peak positive dP/dt , dP/dt_{min} : peak negative dP/dt , EDP: end-diastolic pressure, ESP: end-systolic pressure, Tau: the time constant of LV isovolumic pressure decay (logarithmic method) (197, 247), ED-ES: time interval from end-diastole (ED) to end-systole

(ES), QT: QT interval on surface ECG, QTc: corrected QT interval, TDR: transmural dispersion of repolarization. *P < 0.05 vs. atrial pacing.

Table 7-2. End-systolic strains. Values are transmural average (subepicardium, midwall and subendocardium) \pm SE (n=5). E_{11} : circumferential strain, E_{22} : longitudinal strain, E_{33} : radial strain, E_{12} : circumferential-longitudinal shear strain, E_{23} : longitudinal-radial shear strain, E_{13} : circumferential-radial shear strain, E_{ff} : fiber strain, E_{ss} : sheet strain, E_{nn} : strain normal to the sheet plane, E_{fs} : shear strain within the sheet plane, E_{sn} : sheet shear strain, E_{fn} : fiber-normal shear strain, β : sheet angle, *: P<0.05 vs. Atrial pace.

Figure 7-3. Temporal sequence of each strain component. Values are means \pm SE (n=5). Subepicardium, midwall, and subendocardium represents 25%, 50% and 75% wall depth from the epicardial surface, respectively. The reference state for strain calculation was end-diastole for both atrial pacing (peak of the ECG R-wave) and LV epicardial pacing (V-spike). dP/dt_{max} : the timing of LV peak positive dP/dt , ES: end-systole, EC: early contraction, ER: early relaxation. Note different scales for shear and normal strains.

Figure 7-4. Transmural delay in mechanical activation time (t_m). Values are means \pm SE (n=5). Subepicardium and subendocardium refer to 25% and 75% wall depth, respectively. End-diastole was used as the reference state (time = 0) for both atrial pacing and LV epicardial pacing. Maximum fiber shortening in atrial pacing and LV epicardial pacing was found near end-systole and peak positive dP/dt (dP/dt_{max}), respectively. *: P < 0.05 vs. subepicardium of the same pacing mode, †: P < 0.05 vs. subepicardium of atrial pacing.

Table 7-3. Transmural mechanical activation strains (E'). Values are transmural average (subepicardium, midwall and subendocardium) \pm SE (n=5). *: P<0.05 vs. Atrial pace.

Chapter 8

Global electromechanics in infarct heart

Figure 8-1. Epicardial electrical signals during a cardiac cycle (cycle length = 544 msec, HR = 110 bpm) registered to a short-axis delayed hyperenhancement (DHE) MR image of the LV split into 32 sectors. Regions of bright intensity correspond to MI. In this image, abnormal or delayed activation is seen from sectors 4 through 9, whereas the infarct ranges from sectors 3 through 14.

Table 8-1. Hemodynamic data. Values are mean \pm SE. LVP_{max} : peak LV pressure, dP/dt_{max} : peak positive dP/dt , dP/dt_{min} : peak negative dP/dt , LVEDP: LV end-diastolic pressure, LVESV: LV end-systolic pressure, LVSV: LV stroke volume, LVEF: LV ejection fraction, CO: cardiac output.

Figure 8-2. Short-axis, delayed hyperenhancement (DHE) image of MI from a single animal. Regions of bright intensity correspond to MI. Note multiple interdigitations of viable myocardium within the infarct region.

Figure 8-3. Infarct depth and electrical activation from a single animal. A. Infarct map (in percent depth). B. Isochrone map of electrical activation time (in msec). The area circumscribed by a solid black line represents the right ventricle (RV). The area circumscribed by a solid white line represents the infarct zone in the anterior wall (the infarct zone in the septum is covered by the RV). Pos: posterior wall, Sep: septal wall, Ant: anterior wall, Lat: lateral wall.

Figure 8-4. Quantitative analysis of electrical activation time in each zone (n=6). Electrical activation time (in msec) was significantly delayed in the infarct zone compared with that of the border zone (31 ± 9 vs. 19 ± 2 msec, $P < 0.05$), whereas it was not significantly different between the border zone and the remote zone (19 ± 2 vs. 21 ± 3 msec, $P = \text{n.s.}$).

Figure 8-5. 3-D Displacement map from a single animal. Each arrow represents a displacement vector that points from the end-diastolic to end-systolic configuration. The magnitude of displacement is color-coded. It is clear that the displacement magnitude in the infarct zone in the anteroseptal wall (left side of the figure) is small (purple ~ blue) compared to that of the remote zone in the posterolateral wall (right side of the figure, red ~ yellow).

Figure 8-6. 3-D Strain map from a single animal. The area circumscribed by a solid white line represents the infarct zone. E_{rr} : radial, E_{cc} : circumferential, and E_{ll} : longitudinal strains. The regions of abnormal strains, particularly the longitudinal strain, extended far beyond the infarct zone, and the strains were larger in the epicardium than in the endocardium. Epi: epicardial layer, Endo: endocardial layer.

Figure 8-7. Quantitative analysis of finite strain in each zone (n=6). E_{rr} , E_{cc} and E_{ll} in both the infarct zone and the border zone were significantly smaller than those in the remote zone ($P < 0.05$), and there was no significant difference between the infarct zone and the border zone ($P = \text{n.s.}$). There was a significant transmural gradient between the epicardium and endocardium in E_{rr} , E_{cc} and E_{ll} in the remote zone ($P < 0.05$), and the transmural gradient was lost in both the infarct zone and the border zone.

Chapter 9

Global electromechanics in infarct heart with substrate for sudden cardiac death

Figure 9-1. Overview of data acquisition and processing.

Figure 9-2. The magnitude (A) and the phase (B) images from the cine-DENSE sequence.

Figure 9-3. Image acquisition, displacement and strain calculation using the cine-DENSE sequence.

Figure 9-4. A. Circumferential strain. Circumferential strain ϵ_c describes myocardial shortening or stretch in the circumferential direction. **B. Sample fit of raw circumferential strain data at image frames (+) to 7th-order polynomials (solid line).** A zero strain value (○) was indicates the time of the tag encoding gradient (=22msec after the peak of the ECG-R wave)

to reflect the reference configuration. **C. Mesh reconstruction of LV.** Mesh vertices indicate locations of displacement and strain calculations. There are a total of 144 data points per heart (=24 sectors x 6 short-axis slices).

Figure 9-5. A. Short-axis view of the contrast-enhanced MR image. Regions of high intensity (= light gray) corresponds to MI. **B. Mesh presentation of the MI wall depth (%) in one animal.** Note the MI was mostly transmural (= dark red), and was located in the anteroseptal region.

Figure 9-6. Unipolar electrical recordings from an epicardial sock electrode. A. Normal sinus rhythm, B. Sustained monomorphic VT.

Figure 9-7. Time course of circumferential strain in one animal. The numbers indicate the time from the peak of ECG-R wave. The area circumscribed by a solid line represents MI (>50% wall depth). Note the circumferential length change appears greater than actual change *in vivo*.

Figure 9-8. Average mechanical indices by region (n=8). A. Prestretch (circumferential strain, %), B. Peak prestretch rate (circumferential strain/sec, %/sec), C. Time to onset of shortening (time, msec), D. Time to peak shortening (time, msec), E. Peak shortening (circumferential strain, %), F. Peak shortening rate (circumferential strain/sec, %/sec). The area circumscribed by a solid line represents MI (> 50% wall depth).

Figure 9-9. Comparison of mechanical indices between viable vs. infarct myocardium. These box plots contain the pooled data from all the data points from all animals. The boundary of the box closest to zero indicates the 25th percentile, a line within the box marks the median, and the boundary of the box farthest from zero indicates the 75th percentile. Whiskers above and below the box indicate the 90th and 10th percentiles. *: P<0.05 vs. viable myocardium.

Figure 9-10. Correlation between prestretch and peak shortening rate in the viable myocardium in one animal (r=-0.75, P<0.001).

Figure 9-11. Correlation coefficients for each animal. Individual correlation coefficients are shown in closed (viable myocardium) and open (infarct myocardium) circles, and the open squares indicate mean±SD of the correlation coefficient in each animal. The number of data points per animal (mean±SD) to calculate each correlation coefficient is also shown. The horizontal dashed lines indicate |r|=0.5. TTOS, time to onset of shortening; TTPS, time to peak shortening; PS, peak shortening; PSR, peak shortening rate; ARI, activation recovery interval.

Figure 9-12. Spatial distribution of prestretch and ARI in one animal. The prolate ellipsoid mesh on the left represents prestretch (color-coded in %) derived from the cine-DENSE images, whereas the epicardial mesh on the right represents ARI (color-coded in msec) derived from the electrical sock measurement. The spatial distribution of greater prestretch (red arrow) was very similar to the distribution of longer ARI (black arrow).

Figure 9-13. Correlation between prestretch and ARI in the prestretch region in one animal (r=0.92, P<0.001).